Journal of Sound and Vibration 475 (2020) 115269

Contents lists available at ScienceDirect

Journal of Sound and Vibration

journal homepage: www.elsevier.com/locate/jsvi

Nonlinear analysis of a geared rotor system supported by fluid film journal bearings

Dongil Shin , Alan Palazzolo *

Department of Mechanical Engineering, Texas A&M University, College Station, TX 77840, USA

ARTICLE INFO

Article history:
Received 14 November 2019
Received in revised form 28 January 2020
Accepted 20 February 2020
Available online 25 February 2020
Handling Editor: J. Lam

Keywords:
Nonlinear gear dynamics
Multiple shooting method
Jump phenomena
Multiple co-existing response
Chaos
Journal bearing

ABSTRACT

This paper presents a novel approach for modeling and analyzing a geared rotor-bearing system including nonlinear forces in the gear set and the supporting fluid film journal bearings. The rotordynamics system model has five degrees of freedom that define the transverse displacements of the shaft-gear centerlines and the relative displacement of the gear tooth contact point. The journal bearing nonlinear forces are obtained via a solution of Reynolds equation for lubricant film pressure utilizing the finite element method. Co-existing, steady-state, autonomous and non-autonomous responses are obtained in an accurate and computationally efficient manner utilizing the multiple shooting and continuation algorithms. This yields the full manifolds of the multiple bifurcation system. Chaos is identified with maximum Lyapunov exponents, frequency spectra, Poincaré attractors, etc. The results reveal a dependence of the gear set contact conditions and system nonlinear response characteristics, i.e. jump, co-existing responses, subharmonic resonances and chaos on the choice of journal bearing parameters. The results also show that Hopf bifurcations, which occur along with oil whirl in a journal bearing system, can be attenuated by increasing the gear torque.

1. Introduction

Gearing system speeds and operating torques continue to increase in high-performance machinery. This amplifies the effects of nonlinearities in the gears including tooth backlash and time-varying mesh stiffness. Backlash describes the intentional clearance provided between mating teeth to prevent binding and to include a thin lubricant film between the teeth for heat removal and reduced wear. Backlash causes intermittent loss of contact between the teeth creating a nonlinear force and torque. The mesh stiffness varies periodically with time due to the variation of the number of tooth pairs in contact, and the variation of the point of contact along with the tooth profiles. The time-varying stiffness of the meshing teeth may lead to parametric resonances, which are principal sources of internal excitations and vibrations in gear transmission systems. The backlash forces and time-varying stiffness interact yielding a complex nonlinear, parametrically excited system with both torsional and lateral vibration. Accurate and computationally efficient gear dynamic models, including nonlinear forces and parametric excitations, are required for the effective design of gear sets and the machinery in which they form a critical component.

* Corresponding author.
E-mail addresses: davshin@tamu.edu (D. Shin), a-palazzolo@tamu.edu (A. Palazzolo).

https://doi.org/10.1016/j.jsv.2020.115269

Significant prior research has been performed on the nonlinear dynamic response of geared systems. Kahraman and Singh [1] analyzed the effect of backlash on a single-degree-of-freedom gear model employing both analytical and numerical simulations. They validated their model by comparison with experimental results and found that the nonlinear characteristics caused chaotic and subsynchronous resonance responses. Kahraman and Singh [2] examined interactions between gear backlash nonlinearity and the bearing clearances and identified chaotic and subharmonic responses. Kahraman and Singh [3] included time-varying stiffness and clearance nonlinearity in their numerical model of geared systems and identified strong coupling effects between these characteristics. Blankenship and Kahraman [4] presented an experimental − analytical correlation study of a geared system including backlash nonlinearity and parametric excitation. Their predictions of co-existing solutions with the harmonic balance method were confirmed experimentally. Kahraman and Blankenship [5] observed subharmonic resonances in a geared system experiment, which were demonstrated to be strongly dependent on damping ratio and stiffness variation of the gear mesh. Kahraman and Blankenship [6] experimentally observed chaotic vibration, jump phenomena, and subharmonic response due to parametric and backlash excitations. Ranghothama and Narayanan [7] employed an incremental harmonic balance method, arc-length continuation, Floquet theory, and Lyapunov exponents to examine the bifurcation characteristics of a three-degree-of-freedom geared rotor-bearing model. Theodossiades and Natsiavas [8] introduced a new analytical method for a gear system with time-varying stiffness and backlash using perturbations techniques. Al-shyyab and Kahraman [9,10] investigated the nonlinear response of a multi-mesh gear system using a multi-term harmonic balance method. The effects of gear parameters on the nonlinear behavior were studied for both period-one and sub-harmonic motions. Liu et al. [11] analyzed the effect of gear mesh damping and backlash amplitude on the states of gear meshing and nonlinear behaviors of a gear pair. Yang et al. [12,13] predicted the nonlinear vibration of a gear system subjected to multi-frequency excitations utilizing a multiple time scales method. They confirmed the interaction between different harmonic excitations and the complex nonlinear behaviors caused by the multi-frequency excitations. Yang et al. [14] performed parametric studies to investigate the influence of the contact ratio, spacing error, transmitted load and mesh damping of a gear using a fifth-order Runge-Kutta method. Wang et al. [15] analyzed the effect of modulation internal excitation on the gear system and verified the accuracy of the prediction by comparing its results with the experimental measurements.

Nonlinear vibration in different types of gears has been investigated. Motahar et al. [16] performed a numerical, nonlinear dynamics study of a bevel gear system. Tip and root modifications were introduced to study their influence on gear vibration. Yang and Lim [17] developed a hypoid gear model considering time varying mesh stiffness, backlash nonlinearity and time-varying bearing stiffness. They showed that the backlash nonlinearity could suppress parametric instability induced by the time-varying bearing stiffness, under certain operating conditions. Wang and Lim [18] studied the effect of gear mesh stiffness asymmetry for the drive and coast sides of the hypoid gear system, and confirmed that the mesh stiffness at the drive side has more significant effect on the nonlinear dynamics. Ambarisha and Parker [19] investigated nonlinear dynamics of a planetary gear system. They applied the profile of the time-varying mesh stiffness obtained from a finite element analysis to improve accuracy. Zhao and Ji [20] performed numerical simulations of a wind turbine gearbox having two planetary gear trains. Complex nonlinear responses of the gearbox were shown to result from a time-varying mesh stiffness, backlash nonlinearity and static transmission error. Xinghui et al. [21] analyzed parametric resonance of a planetary gear subjected to speed fluctuations. The gear model considers time-varying mesh stiffness, and the instability boundaries for the fundamental and combinations resonances were derived based on a perturbation analysis.

Some researchers have explored approaches to suppress vibrations induced by gear nonlinearities. Cheon's [22] simulation study investigated the effect of a one-way clutch to reduce the dynamic transmission error of a geared system. Cheon [23] employed a phasing approach to reduce time-varying mesh stiffness and the resulting vibration, especially at the fundamental resonance.

Stochastic methods have been applied to study the effects of uncertainty in gear parameters. Bonori and Pellicano [24] utilized a stochastic model to analyze the effect of manufacturing error on nonlinear gear dynamics and showed that this could induce chaotic vibrations in the gear system. Wei et al. [25] included modeling uncertainties of a gear system, such as mesh stiffness and damping, and determined the resulting response levels using an interval harmonic balance method.

Various analytical and modeling methods have been applied to gear dynamics simulation. Kim et al. [26] investigated the effect of smoothing functions on clearance nonlinearity of an oscillator and showed how the adjustment of a regulating factor associated with the smoothing functions yielded more reliable predictions. Farshidianfar and Saghafi [27] applied a Melnikov type analysis to investigate homoclinic bifurcations and chaotic responses in a geared system. Gou et al. [28] employed a cell mapping theory to analyze the multi-parameter coupling characteristics of gear parameters. Li et al. [29] used an incremental harmonic balance method to analyze gear systems with internal and external periodic excitations.

Hydrodynamic journal bearings are widely employed in geared systems with high speed and load requirements due to their relatively high stiffness and damping. Theodossiades and Natsiavas [30] investigated the effect of gear and journal bearing parameters on bifurcation, chaos and oil whirl. They represented the journal bearing force with a finite-length impedance method. Baguet and Jacquenot [31] developed a finite element shaft model to study the interactions between a helical gear and a finite-length bearing and showed that a linearized bearing coefficient model does not provide accurate predictions of gear vibrations, especially at high speed and load conditions. Fargère and Velex [32] investigated the effects of the bearing oil inlet location and thermal response on the gear system dynamics. These effects change the journal static equilibrium position, which in turn alters the dynamic response of the system. Liu et al. [33] studied the interactions between tooth wedging effect and journal bearing clearance using the approximate short journal bearing theory. Simulation results showed that varying the operating speed or applied torque may cause the occurrence of oil whirl response of the rotordynamic systems. The effect of tooth wedging on the vibration level of the geared-rotor system is also presented.

Kim and Palazzolo [34,35] employed shooting with deflation to study the nonlinear response of a Jeffcott rotor supported by floating ring bearings. The effects of changing parameters such as bearing length-to-diameter (L/D) ratio and including the thermal effect of the lubricant were presented. Kim and Palazzolo [36] studied the bifurcation of a heavily loaded rotor with five-pad tilting pad bearings. A shooting/arc-length continuation approach was utilized to obtain quasi-periodic and chaotic motions, the latter being confirmed by maximum Lyapunov exponents.

Prior models for coupled gearset-bearing vibration generally utilized lower fidelity or steady-state bearing models, and presented results in less rigorous nonlinear dynamics formats. This may have been motivated by the high computational expense of employing higher fidelity bearing models and presenting results in advanced nonlinear dynamics formats. Bearing forces were typically represented with linear spring and damping constants, or were obtained using short bearing theory, with highly simplified oil film cavitation models. The simplified approaches may lead to significant prediction error especially for steady-state responses with orbits that are relatively large (>15%) with respect to the bearing clearance. The present approach provides a highly accurate, finite element-based solution of the finite-length, Reynold's equation accounting for cavitation at each time step in the numerical integration. Additionally, results are presented in advanced nonlinear dynamics formats including bifurcation diagrams, maximum Lyapunov exponent plots, and Poincaré attractor plots. Computation time is held within practical limits utilizing multiple shooting and continuation algorithms, and with the use of embedded C++ components in the MATLAB code, and parallel processing.

The highlight and original contribution of the work is to provide a computationally efficient, high fidelity and rigorously presented modeling approach for the dynamics of the five-degree-of-freedom dual shaft-gear pair system supported on fluid film bearings. This approach involves finite-length bearing models, advanced multiple shooting and continuation methods, gear flexibility and transmission error effects, bifurcation and Poincaré attractor diagrams, and maximum Lyapunov exponents for identifying chaotic behavior. Finally, this approach is applied to parametric studies with varying journal bearing and gear mesh stiffness parameters.

2. Modeling of a geared rotor system supported by fluid film journal bearings

2.1. Five-degree-of-freedom gear-bearing-rotor model

Fig. 1 shows a centered gear pair attached to parallel rotors that are each supported by fluid film journal bearings. The model is composed of two rigid rotors having mass elements m_i, radii R_i and polar moments of inertia J_i. The subscript i denotes the driving ($i = 1$) and driven ($i = 2$) geared rotors.

An external torque T_1 is applied to the driving gear. A nonlinear mesh coupling consisting of tooth backlash and time-varying stiffness is modeled to transmit torque between driving and driven gears. The motion coordinates for the model include $(\theta_1, \theta_2, x_1, x_2, y_1, y_2)$ as shown in Fig. 2.

The dynamic transmission error (DTE), $\delta(t)$ is given by

$$\delta(t) = R_1\theta_1 - R_2\theta_2 + x_1 \sin(\alpha) - x_2 \sin(\alpha) + y_1 \cos(\alpha) - y_2 \cos(\alpha) - e_r(t) \tag{1}$$

where $e_r(t)$ represents the static transmission error. The analytical description of the time-varying mesh stiffness and the static transmission error can be expressed in the form of Fourier series as [3]

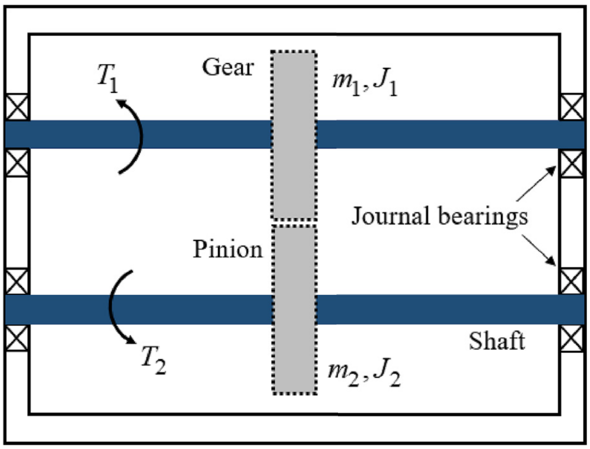

Fig. 1. Gear set supported by hydrodynamic journal bearings.

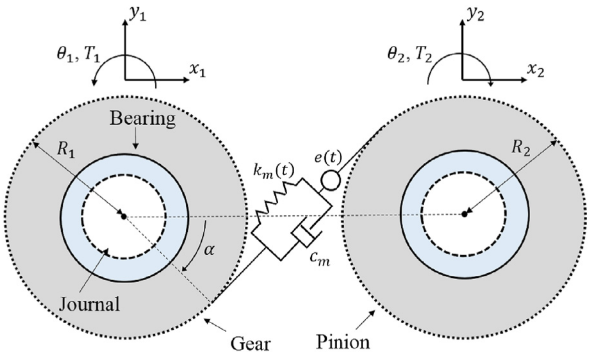

Fig. 2. Spur gear pair model including hydrodynamic journal bearings.

$$
\begin{aligned}
k_m(t) &= k_0 + \sum_{i=1}^{\infty} s_i k_0 \cos(i\omega_g t - \varphi_i) \\
e_r(t) &= e_0 + \sum_{j=1}^{\infty} p_j e_0 \cos(j\omega_g t - \psi_j)
\end{aligned}
\tag{2}
$$

where k_0 is a mean mesh stiffness, e_0 is a mean static transmission error, and s_i and p_j are the amplitude of the Fourier series components. The phase angles of the Fourier series are represented by φ_i and ψ_j, respectively.

The term ω_g is the gear mesh frequency represented by

$$\omega_g = N_i \omega_i \tag{3}$$

where N_i is the number of gear teeth, ω_i is rotor operating frequency and $i = 1, 2$. For this study $\omega_1 = \omega_2 = \omega$ is used, which follows the convention in the related literature [33]. The pressure angle α is assumed to remain constant during operation. Plain journal bearings support both rigid shafts, and their nonlinear fluid film force models are explained in section 2.2.

As noted in Ref. [26], a tooth backlash model defined with a piecewise linear function in the governing nonlinear differential equations may result in convergence difficulties when employing a Newton-Raphson method. Therefore, the following smoothening function presented in the same reference is also used in the present study.

$$\rho(t) = \frac{1}{2}\{(\delta(t) - b)[1 + \tanh(\sigma(\delta(t) - b))]\} + \frac{1}{2}\{(\delta(t) + b)[1 + \tanh(-\sigma(\delta(t) + b))]\} \tag{4}$$

where $\rho(t)$ represents relative gear mesh displacement considering backlash, b is the half-length of the tooth backlash amplitude ($b = \frac{b_0}{2}$) and σ is a modulating factor which affects the accuracy of the backlash representation and convergence [26]. The value $\sigma = 100$ is selected for this study.

The coupling force between the driving and driven gear mesh is given by

$$F_{m0} = k_m(t)\delta(t) + c_m\dot{\delta}(t) \tag{5}$$

where c_m represents mesh damping, and it is assumed to be constant in this study. $\delta(t)$ represents the dynamic transmission error in Eq. (1), and $\dot{\delta}(t)$ is its derivative.

The equations of motion for the six-degree-of-freedom gear-bearing rotor system are

$$
\begin{aligned}
&J_1\ddot{\theta}_1 + k_m(t)(R_1\theta_1 - R_2\theta_2 + x_1\sin(\alpha) - x_2\sin(\alpha) + y_1\cos(\alpha) - y_2\cos(\alpha) - e_r(t))R_1 + c_m\dot{\delta}(t)R_1 = T_1 \\
&J_2\ddot{\theta}_2 - k_m(t)(R_1\theta_1 - R_2\theta_2 + x_1\sin(\alpha) - x_2\sin(\alpha) + y_1\cos(\alpha) - y_2\cos(\alpha) - e_r(t))R_2 - c_m\dot{\delta}(t)R_2 = -T_2 \\
&m_1\ddot{x}_1 + k_m(t)(R_1\theta_1 - R_2\theta_2 + x_1\sin(\alpha) - x_2\sin(\alpha) + y_1\cos(\alpha) - y_2\cos(\alpha) - e_r(t))\sin(\alpha) + c_m\dot{\delta}(t)\sin(\alpha) = F_{b1x} \\
&m_1\ddot{y}_1 + k_m(t)(R_1\theta_1 - R_2\theta_2 + x_1\sin(\alpha) - x_2\sin(\alpha) + y_1\cos(\alpha) - y_2\cos(\alpha) - e_r(t))\cos(\alpha) + c_m\dot{\delta}(t)\cos(\alpha) = F_{b1y} - m_1 g \\
&m_2\ddot{x}_2 - k_m(t)(R_1\theta_1 - R_2\theta_2 + x_1\sin(\alpha) - x_2\sin(\alpha) + y_1\cos(\alpha) - y_2\cos(\alpha) - e_r(t))\sin(\alpha) - c_m\dot{\delta}(t)\sin(\alpha) = F_{b2x} \\
&m_2\ddot{y}_2 - k_m(t)(R_1\theta_1 - R_2\theta_2 + x_1\sin(\alpha) - x_2\sin(\alpha) + y_1\cos(\alpha) - y_2\cos(\alpha) - e_r(t))\cos(\alpha) - c_m\dot{\delta}(t)\cos(\alpha) = F_{b2y} - m_2 g
\end{aligned}
\tag{6}
$$

By replacing the term $k_m(t)(R_1\theta_1 - R_2\theta_2 + x_1\sin(\alpha) - x_2\sin(\alpha) + y_1\cos(\alpha) - y_2\cos(\alpha) - e_r) + c_m\dot{\delta}(t)$ with F_{m0}, the equations become

$$\begin{aligned}
&J_1\ddot{\theta}_1 + R_1 F_{\mathrm{m0}} = T_1\\
&J_2\ddot{\theta}_2 - R_2 F_{\mathrm{m0}} = -T_2\\
&m_1\ddot{x}_1 + F_{\mathrm{m0}}\sin(\alpha) = F_{\mathrm{b1x}}\\
&m_1\ddot{y}_1 + F_{\mathrm{m0}}\cos(\alpha) = F_{\mathrm{b1y}} - m_1 g\\
&m_2\ddot{x}_2 - F_{\mathrm{m0}}\sin(\alpha) = F_{b2x}\\
&m_2\ddot{y}_2 - F_{\mathrm{m0}}\cos(\alpha) = F_{b2y} - m_2 g
\end{aligned} \tag{7}$$

where F_{bix} and F_{biy} represents the ith bearing forces in the x and y directions, and $m_1 g$ and $m_2 g$ terms represent gravity forces. By multiplying each of equations with R_1 and R_2, the first two become

$$\begin{aligned}
&J_1 R_1\ddot{\theta}_1 + R_1{}^2 F_{m0} = R_1 T_1\\
&J_2 R_1\ddot{\theta}_2 - R_2{}^2 F_{m0} = -R_1 T_2
\end{aligned} \tag{8}$$

Divide the two equation with J_1 and J_2 respectively, and then subtracting the second equation from the first one, to obtain

$$R_1\ddot{\theta}_1 - R_1\ddot{\theta}_2 + \left(\frac{R_1{}^2}{J_1} + \frac{R_2{}^2}{J_2}\right)F_{\mathrm{m0}} = \frac{R_1}{J_1}T_1 + \frac{R_2}{J_2}T_2 \tag{9}$$

Substituting $p = R_1\theta_1 - R_2\theta_2$ and manipulating the equation yields

$$\ddot{p} + \left(\frac{J_2 R_1{}^2 + J_1 R_2{}^2}{J_1 J_2}\right)F_{\mathrm{m0}} = \frac{R_1}{J_1}T_1 + \frac{R_2}{J_2}T_2 \tag{10}$$

Dividing through by $\left(\frac{J_2 R_1{}^2 + J_1 R_2{}^2}{J_1 J_2}\right)$ yields

$$\left(\frac{J_1 J_2}{J_2 R_1{}^2 + J_1 R_2{}^2}\right)\ddot{p} + F_{\mathrm{m0}} = \left(\frac{J_1 J_2}{J_2 R_1{}^2 + J_1 R_2{}^2}\right)\left(\frac{R_1}{J_1}T_1 + \frac{R_2}{J_2}T_2\right) \tag{11}$$

Substitute J_e for $\left(\frac{J_1 J_2}{J_2 R_1{}^2 + J_1 R_2{}^2}\right)$ to obtain

$$J_e\ddot{p} + F_{\mathrm{m0}} = T_e \tag{12}$$

where $T_e = J_e\left(\frac{R_1}{J_1}T_1 + \frac{R_2}{J_2}T_2\right)$ is an equivalent input torque term.

The term $\delta(t)$ was inserted into Eq. (4) to include the backlash nonlinearity effect. Then, from Eqs. (4) and (5), the gear meshing force including the backlash nonlinearity effect becomes

$$F_m = k_m\rho(t) + c_m\dot{\delta}(t) \tag{13}$$

Finally, the equations including the backlash nonlinearity, time-varying mesh stiffness and the static transmission error become

$$\begin{aligned}
&J_e\ddot{p} + F_m = T_e\\
&m_1\ddot{x}_1 + F_m\sin(\alpha) = F_{\mathrm{b1x}}\\
&m_1\ddot{y}_1 + F_m\cos(\alpha) = F_{\mathrm{b1y}} - m_1 g\\
&m_2\ddot{x}_2 - F_m\sin(\alpha) = F_{\mathrm{b2x}}\\
&m_2\ddot{y}_2 - F_m\cos(\alpha) = F_{\mathrm{b2y}} - m_2 g
\end{aligned} \tag{14}$$

where J_e is the equivalent inertia of two gears, i.e. $\left(\frac{J_1 J_2}{J_2 R_1{}^2 + J_1 R_2{}^2}\right)$. The torsional natural frequency ω_n of the system is defined as $\sqrt{\frac{k_0}{J_e}}$.

For validation purposes, the simulation result are compared with experimental measurements [4] in Fig. 3. The experiment was conducted using relatively stiff ball bearings so the x and y journal motions are assumed fixed in the simulation. The gear parameters for backlash, Fourier coefficients of time varying mesh stiffness and amplitude of static transmission error

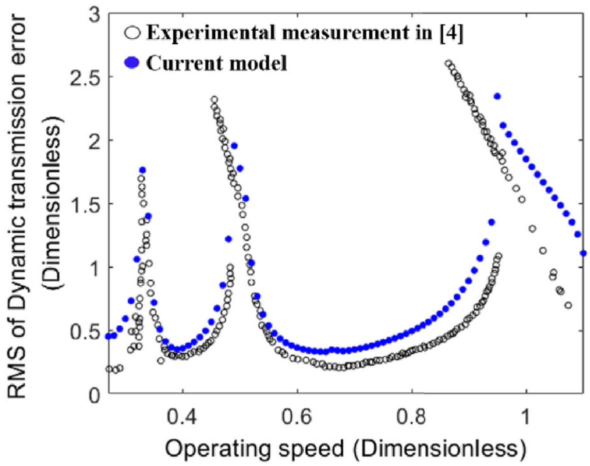

Fig. 3. Comparison of dynamic transmission error with experimental measurements in Ref. [4] (Ref. [37]).

Table 1
Comparison of calculated natural frequencies with [15].

	Calculated natural frequencies in Ref. [15]	Natural frequencies based on current model
1st mode	0 Hz	0 Hz
2nd mode	1149 Hz	1149.3 Hz
3rd mode	1293 Hz	1293.6 Hz
4th mode	1604 Hz	1604.3 Hz
5th mode	1799 Hz	1799.1 Hz
6th mode	5043 Hz	5043.7 Hz

from Ref. [4] are employed in the simulation. The root mean square (RMS) value of the dynamic transmission error is plotted with respect to operating speed, showing good agreement between prediction and test results.

Table 1 provides a second validation case through comparison of the five-degree-of-freedom gear-bearing dynamic model's predicted natural frequencies with those provided in Ref. [15]. Since natural frequencies are characteristics of a linear model, the backlash and time varying stiffness were omitted and the bearing forces were represented by the stiffness and damping provided in the reference. The correlation is shown in the table and confirms excellent agreement.

2.2. Finite element model of plain journal bearing

The Reynolds equation [34] for an incompressible lubricant combines the fluid continuity and momentum equations into a partial differential equation for film pressure, and is given by

$$\frac{\partial}{\partial\theta}\left(\frac{h^3}{12\mu}\frac{\partial p}{\partial\theta}\right)+\frac{\partial}{\partial z}\left(\frac{h^3}{12\mu}\frac{\partial p}{\partial z}\right)=\frac{R_J\omega_J}{2}\frac{\partial h}{\partial\theta}+\frac{\partial h}{\partial t} \tag{15}$$

where ω_J is the rotating speed of the journal, and R_J and μ represent the radius of the journal and the viscosity of the lubricant, respectively. The centers of the bearing and the journal are O_B and O_J in Fig. 4, respectively.

The displacements of the journal center relative to the bearing center in the x and y directions are x_J and y_J, respectively, and p is the pressure in the lubricant film. Expressions for fluid film thickness h and its derivative $\frac{\partial h(\theta)}{\partial t}$ at θ are given by

$$\begin{aligned} h(\theta) &= C_B - x_J\cos\theta - y_J\sin\theta \\ \frac{\partial h(\theta)}{\partial t} &= -\dot{x}_J\cos\theta - \dot{y}_J\sin\theta \end{aligned} \tag{16}$$

where C_B represents the bearing radial clearance.

The mathematical model assumes rigid shafts and rigid attachments between the bearings and ground. Therefore, the journal motions x_J and y_J are identical to their respective gear centerline motions. Thus x_1, y_1 are identical to x_{J1} and y_{J1}, and x_2, y_2 are identical to x_{J2} and y_{J2}.

The finite element mesh of a fluid film is illustrated in Fig. 5. The coordinate θ corresponds to the circumferential direction of the film and the direction of rotation is from the left (θ_B) to the right (θ_E). The axial coordinate is represented with z and only

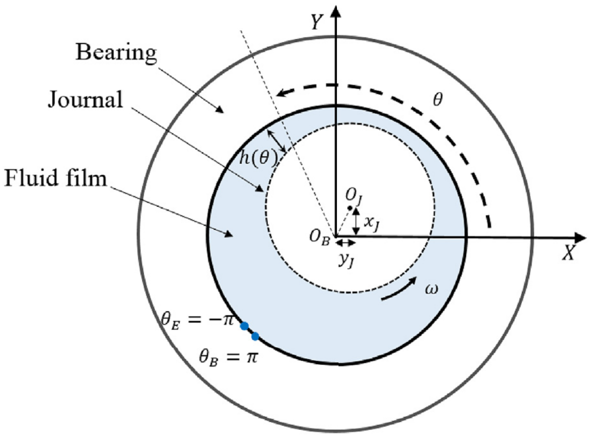

Fig. 4. Axial mid-plane section of a journal bearing.

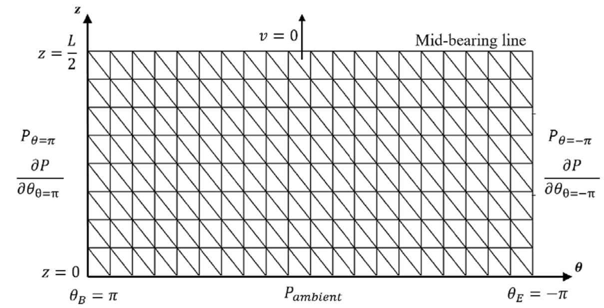

Fig. 5. Mesh and boundary conditions for finite element journal bearing film model.

a half-length ($\frac{L}{2}$) of the film is modeled due to its symmetry. The pressure on the bottom ($z = 0$) side of the mesh are set to ambient pressure P_{ambient}. Continuous pressure and flow condition are imposed on the left and right sides of the mesh. The zero-flow condition at the symmetric side ($z = \frac{L}{2}$) and the continuous pressure and pressure gradient conditions at left/right sides are applied as follows

$$v_{\mathrm{z=L/2}} = 0,\ P_{\theta=\pi} = P_{\theta=-\pi},\ \frac{\partial p}{\partial \theta_{\theta=\pi}} = \frac{\partial p}{\partial \theta_{\theta=-\pi}} \tag{17}$$

The Reynolds equation is solved with a mesh of triangular simplex finite elements, which interpolate the two-dimensional pressure distribution in the film domain. The instantaneous reaction force on a journal is obtained by integrating the pressure distribution. Considering that symmetry condition the journal reaction force becomes

$$F_{\mathrm{bi}} = \begin{Bmatrix} F_{\mathrm{bix}} \\ F_{\mathrm{biy}} \end{Bmatrix} = 2 \int_{0}^{L/2} \int_{-\pi}^{\pi} p \begin{Bmatrix} \cos\theta \\ \sin\theta \end{Bmatrix} d\theta dz \tag{18}$$

3. Nonlinear steady-state solution methods

3.1. Multiple shooting method

The shooting method (SM) is a numerical procedure that utilizes an iterative algorithm and numerical integration of the nonlinear differential equations to locate co-existing, periodic equilibrium states. The SM provides a guided iterative search to locate the state vectors that repeat after a specified, or unknown in the case of autonomous systems, period. The single shooting method (SSM) is widely used in nonlinear dynamics research because of its simplicity. However, SSM may experience convergence problems, especially at saddle-node points. Multiple shooting methods (MSM) improves the numerical stability of the SSM by dividing time intervals into smaller ones. Compared to SSM, the MSM shows more robust convergence to periodic states and is less sensitive to the selection of initial state guesses. In addition, MSM is more suitable for parallel computing, thus making it desirable for systems with a large number of degrees of freedom.

The MSM algorithm is explained in this section. The non-autonomous nonlinear equations of motion can be represented by the first order form as

$$\frac{d}{d\tau}\mathbf{x} = \mathbf{x}' = \mathbf{h}(\mathbf{x}, \tau, p)(n \times 1) \tag{19}$$

where $\mathbf{x}$ is a state vector, τ is an explicit time variable in the forcing term and p represents the physical parameters of a system. The period of the steady-state harmonic response defined by a user is represented by the minimum period P_F and a rational number R in the non-autonomous case

$$P_R = RP_F \tag{20}$$

The solution at the end of the period P_R is represented

$$\mathbf{x}_{\mathbf{T_R}} = \mathbf{x}(\tau = P_R, \mathbf{x}(0) = \mathbf{x_0}) \tag{21}$$

where x_0 is the initial condition state vector. If x_0 is a solution on an orbital equilibrium state of the period P_R, it will result that

$$\begin{aligned} &\mathbf{x}_{\mathbf{T_R}} = \mathbf{x}(\tau = P_R, \mathbf{x}(0) = \mathbf{x_0}) = \mathbf{x_0} \\ &\mathbf{x_0} = \mathbf{g} + \mathbf{e} \end{aligned} \tag{22}$$

where g is a user-defined guess of initial conditions, and e is an error term.

Unlike SSM which requires the single end-point constraint ($\mathbf{x}_{T_R} = \mathbf{x}_0$) as explained above, MSM divides P_R into smaller intervals and generates multiple constraints as follows:

$$\begin{aligned} &\mathbf{x}_{P_1} = \mathbf{x}(\tau = P_1, \mathbf{x}(0) = \mathbf{x}_0) = \mathbf{x}_1 \\ &\mathbf{x}_{P_2} = \mathbf{x}(\tau = P_2, \mathbf{x}(0) = \mathbf{x}_1) = \mathbf{x}_2 \\ &\vdots \\ &\mathbf{x}_{P_{m-1}} = \mathbf{x}(\tau = P_{m-1}, \mathbf{x}(0) = \mathbf{x}_{m-2}) = \mathbf{x}_{m-1} \\ &\mathbf{x}_{P_m} = \mathbf{x}(\tau = P_m, \mathbf{x}(0) = \mathbf{x}_{m-1}) = \mathbf{x}_m = \mathbf{x}_0 \end{aligned} \tag{23}$$

where divided time intervals are $0 = P_0 < P_1 < \cdots < P_m = P_R$. Note that m is the number of time intervals defined by a user. A multi-dimensional Newton-Raphson method is applied to update $\mathbf{x}_0$.

For an autonomous system, the additional phase condition should be defined since the point of the periodic solution at a specific time is not unique. In this study, a phase condition that sets the DTE from Eq. (1) as zero is used [42].

$$\begin{aligned} &\mathbf{H}(\mathbf{x}_0, P_A) = \mathbf{g}(\mathbf{x}_0, P_A) - \mathbf{x}_0 = 0 \\ &\mathbf{c}(\mathbf{x}_0) = 0 \end{aligned} \tag{24}$$

where P_A is a period of an autonomous system orbit to be identified along with an initial condition $\mathbf{x}_0$.

3.2. Arc-length continuation

The shooting method may take considerable computation time, especially when plotting co-existing solution loci versus system parameters. "Continuation algorithms" have been developed to generate the loci (branch plots) with significantly increased efficiency relative to conducting independent SM searches for each parameter value. The Arc-length Continuation (AC) method [42] is applied in this research. AC provides robust solution searches even in high curvature regions by utilizing the trajectory of the solution curves along an arc-length as shown in Fig. 6.

An additional unknown ω is involved in the iteration search. The next solution is

$$\begin{Bmatrix} \tilde{\mathbf{g}}_n^{i+1} \\ \omega_n^{i+1} \end{Bmatrix} = \begin{Bmatrix} \tilde{\mathbf{g}}_n^{i} \\ \omega_n^{i} \end{Bmatrix} + \begin{bmatrix} \tilde{\mathbf{J}}_g^i & \mathbf{J}_\omega^i \\ \frac{\partial \mathbf{k}_n^{iT}}{\partial \mathbf{x}} & \frac{\partial \mathbf{k}_n^{i}}{\partial \omega} \end{bmatrix} \begin{Bmatrix} -\mathbf{f}\left(\tilde{\mathbf{g}}_n^i, \omega_n^i\right) \\ -\mathbf{q}\left(\tilde{\mathbf{g}}_n^i, \omega_n^i, s\right) \end{Bmatrix} \tag{25}$$

where ω and s are operating parameters and arc-length of the solution curve, respectively, n is a current step number, $\mathbf{J}_\omega$ is Jacobian matrix with regard to ω, and k is the constraint imposed on the solution procedures as

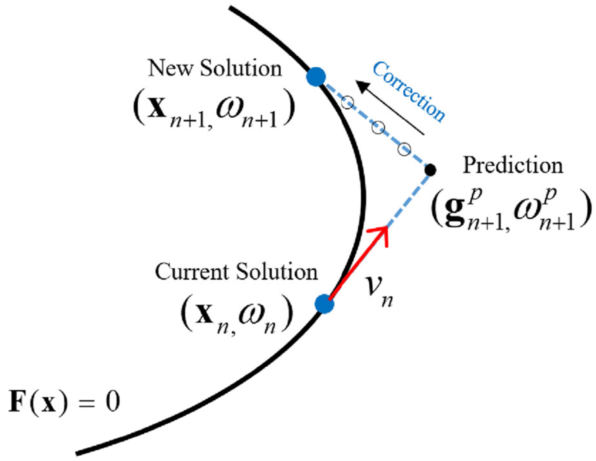

Fig. 6. Pseudo Arc-length Continuation method.

$$\mathbf{k}(\mathbf{x}, \omega, s) = \nu \left\| \tilde{\mathbf{g}}^i_{n+1} - \tilde{\mathbf{g}}_n \right\|_2^2 + \left(\omega^i_{n+1} - \omega_n \right)^2 - (\Delta s)^2 \tag{26}$$

where ν is a relaxation factor, and Δs is an arc-length.

Then Newton-Raphson iteration is performed until the convergence criteria are satisfied. A continuation of periodic solution searches is carried out to plot a frequency response in the excitation frequency range of interest, including bifurcation points. The phase condition in Eq. (24) is added to Eq. (25) for the autonomous system continuation algorithm.

3.3. Stability identification based on the shooting method

The Jacobian matrix of the shooting method is calculated to determine the local stability of periodic solutions. More specifically, the eigenvalues of the Jacobian matrix at a steady-state solution identifies the solution's stability and its bifurcation type. Perturbed solutions are computed to generate the Jacobian matrix entries. The system is considered unstable if the maximum magnitude of the eigenvalues is larger than unity.

3.4. Lyapunov exponents for identifying chaos

Various approaches are used to identify the presence of chaos in the response of a nonlinear dynamical system. The most widely used approach is to calculate Maximum Lyapunov exponent (MLE, $\mu_{\max}$). Lyapunov exponents indicate the rate of separation of two infinitesimally close trajectories in the local phase space [42]. A total of n initial separation vectors with different directions are used for a system with n states, to obtain a spectrum of n Lyapunov exponents (LE, $\mu_i (i = 1, 2, \ldots, n)$) for calculating the rates of separation. The simultaneous numerical integrations of nonlinear differential equations and linearized form of them are required for the MLE calculation.

$$\text{Nonlinear differential equations}: \ \dot{\mathbf{x}} = \mathbf{g}(\mathbf{x}) \tag{27}$$

$$\text{Linearized form of Eq. (27)}: \dot{\boldsymbol{\beta}} = \mathbf{L}(\boldsymbol{\beta}) \tag{28}$$

The actual and linearized trajectories with perturbed initial conditions are calculated from Eq. (27) and Eq. (28), respectively, at various times along the nonlinear system trajectory. Deviation distances are obtained from the difference between the nonlinear trajectory and linearized trajectories.

$$\boldsymbol{\Delta}(t) = \sqrt{\delta\mathbf{x}_1^2 + \delta\mathbf{x}_1^2 + \cdots + \delta\mathbf{x}_n^2} \tag{29}$$

An appropriate time interval t_f is selected for the numerical integrations to avoid a numerical error. Sets of orthonormalized perturbed vectors are obtained from a Gram-Schmidt procedure as

$$\tilde{\beta}_1=\frac{\beta_1\left(t_f\right)}{\left\|\beta_1\left(t_f\right)\right\|},\ \tilde{\beta}_2=\frac{\beta_2\left(t_f\right)-\left(\beta_2\left(t_f\right)\cdot\tilde{\beta}_1\right)\tilde{\beta}_1}{\left\|\beta_2\left(t_f\right)-\left(\beta_2\left(t_f\right)\cdot\tilde{\beta}_1\right)\tilde{\beta}_1\right\|},\ \text{and}\ \tilde{\beta}_m=\frac{\beta_m\left(t_f\right)-\sum_{i=1}^{m-1}\left(\beta_m\left(t_f\right)\cdot\tilde{\beta}_i\right)\tilde{\beta}_i}{\left\|\beta_m\left(t_f\right)-\sum_{i=1}^{m-1}\left(\beta_m\left(t_f\right)\cdot\tilde{\beta}_i\right)\tilde{\beta}_i\right\|} \tag{30}$$

After conducting the integrations of Eqs. (28)–(30) for r times, the Lyapunov exponents are obtained as

$$\mu_i=\frac{1}{rt_f}\sum_{k=1}^{r}\ \ln\left(\Delta_i^k(t_k)\right) \tag{31}$$

where $\Delta_i^k(t_k)$ is the denominator of the orthonormal vector β_i^k, k denotes the k_{th} time step and i represents ith vector element.

The MLE is used as a quantitative measure to determine the chaotic response of a nonlinear dynamical system as follows.

$$\begin{aligned}
&\bullet\quad \mu_{\max}>0:\ \text{System is chaotic (necessary but not a sufficient condition for chaos)}\\
&\bullet\quad \mu_{\max}<0:\ \text{System attracts to a fixed point or a stable periodic orbit (asymptotically stable)}\\
&\bullet\quad \mu_{\max}=0:\ \text{The orbit is quasi}-\text{periodic}
\end{aligned} \tag{32}$$

4. Numerical example

The five-degree-of-freedom geared rotor-bearing model of Fig. 2 and Eq. (14) is utilized to demonstrate various nonlinear phenomena induced by gear and journal bearing nonlinearities. The multiple shooting/continuation method and Lyapunov exponents discussed in section 3 are utilized along with direct numerical integration. MATLAB ODE15s was used with a relative tolerance of 10^{-9} for computing the Jacobian matrix in the shooting/continuation procedure. Embedded C++ coding and parallel processing are utilized in the MATLAB program to accelerate the execution. The results are divided into 3 sections (1) parametric resonances/jump phenomena and the effect of journal bearing parameter variations on those phenomena, and (2) chaotic responses due to gear nonlinearity and the effect of journal bearing parameters on the responses, and (3) the effect of gear mesh stiffness on the hydrodynamic stability of the gear system supported by journal bearings. Solid and dashed lines indicate stable and unstable responses, respectively in all figures. Table 2 summarizes the parameters of the spur gear pair and journal bearings used in this study.

4.1. Parametric resonances and jump phenomenon

This section presents results for parametric instability, including fundamental and subharmonic resonances induced by time varying mesh stiffness. Both the fundamental and subharmonic resonances are parametric resonances since they are removed when the time varying component of the gear mesh stiffness is removed. Parametric resonance and jump phenomena of a spur gear system with backlash nonlinearity and time-varying mesh stiffness were treated in Refs. [1–8] and more recently in Refs. [9–15]. However, the effects of journal bearing parameters on the nonlinear response of the geared system needs further investigation. Parametric instability of the fundamental and double-period subharmonic frequencies is presented below including journal bearing effects. Applied torque input is considered as an excitation source, and time-

Table 2
Parameters of the spur gear pair and journal bearings.

Gear parameters	
Mass	$m_1 = m_2 = 9.3276$ kg
Moment of inertia	$J_1 = J_2 = 0.03187$ kg·m^2
Radius of gears	$R_1 = R_2 = 0.0982$ m
Pressure angle	$\alpha = 20°$
Backlash amplitude	$b_0 = 100$ μm
Mean mesh (tooth) stiffness	$k_0 = 1e8$ N/m
Mesh damping ratio	$\zeta_m = 0.01-0.025$
Number of gear teeth	$N_1 = N_2 = 28$
Applied torque (T_1)	100–3000 N m
Journal bearing parameters	
Bearing diameter	$D_B = 0.092$ m
Bearing clearance	$C_B = 74-184$ μm
Bearing L/D ratio	0.3–2
Lubricant viscosity	$\mu = 10-90$ mPa s

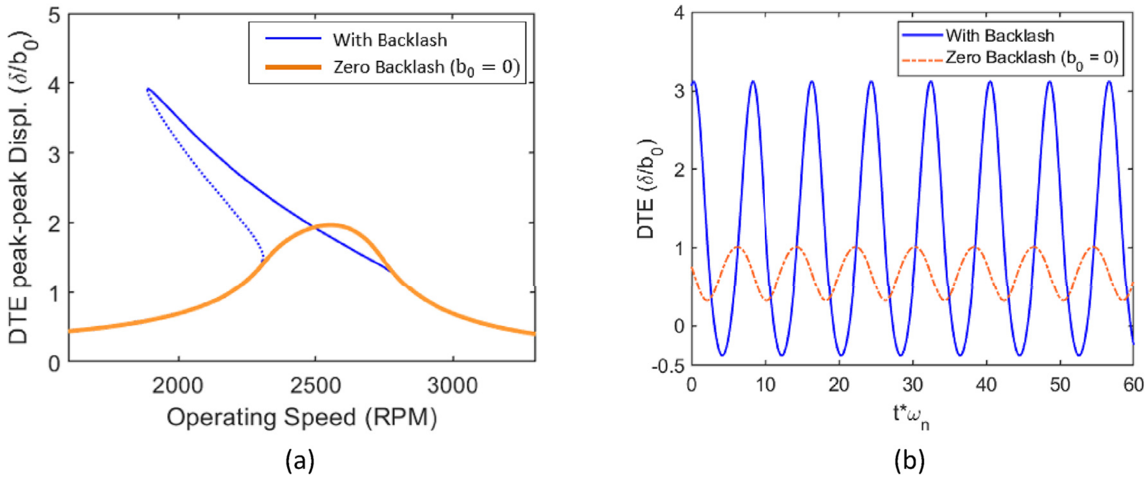

Fig. 7. Effect of backlash (a) peak-peak displacement of DTE (b) time response at 2000 rpm.

varying mesh stiffness with the frequency corresponding to gear mesh frequency ω_g in Eq. (3) is included. No imbalance excitation and static transmission error $e_r(t)$ in Eq. (2) are applied in this section. The non-autonomous, multiple shooting/continuation methods in section 3 are applied to the system equations to analyze the influence of journal bearing parameters on nonlinear responses. Only the first Fourier coefficient of the time-varying mesh stiffness s_1 in Eq. (2) was included, and it was set equal to 0.2, since values from 0.1 to 0.3 are employed in the literatures [1–15]. The bearing L/D ratio is 1, the radial clearance is 105 μm, the lubricant viscosity is 30 mPa s, and an applied torque of 1250 N m is used for the nominal values of the simulation. Each parameter is varied to investigate its effect on the softening effect due to gear nonlinearities.

Direct numerical integrations with initial conditions determined from the shooting/continuation procedure are performed to obtain peak-to-peak displacement amplitude vs. rotor operating speed plots. At the same time, the stability of the periodic solutions is presented and obtained from the shooting method's Jacobian matrix eigenvalues.

4.1.1. Fundamental resonance

Fig. 7 shows the response amplitude regarding operating speed for the non-dimensional peak-to-peak displacements of DTE ($\frac{\delta}{b_0}$) where δ is defined from Eq. (1). The applied torque is 1100 N m in this case. The linear system resonance will occur when the gear mesh frequency $\omega_g = N\omega = \omega_n = \sqrt{\frac{k_0}{J_e}}$. This occurs at around 2500 rpm in this case.

Including backlash causes a softening effect related left-leaning backbone curve with an unstable branch occurring between 1800 and 2300 rpm in Fig. 7(a). Multiple co-existing solutions are seen to occur when the rotor speed is in the vicinity

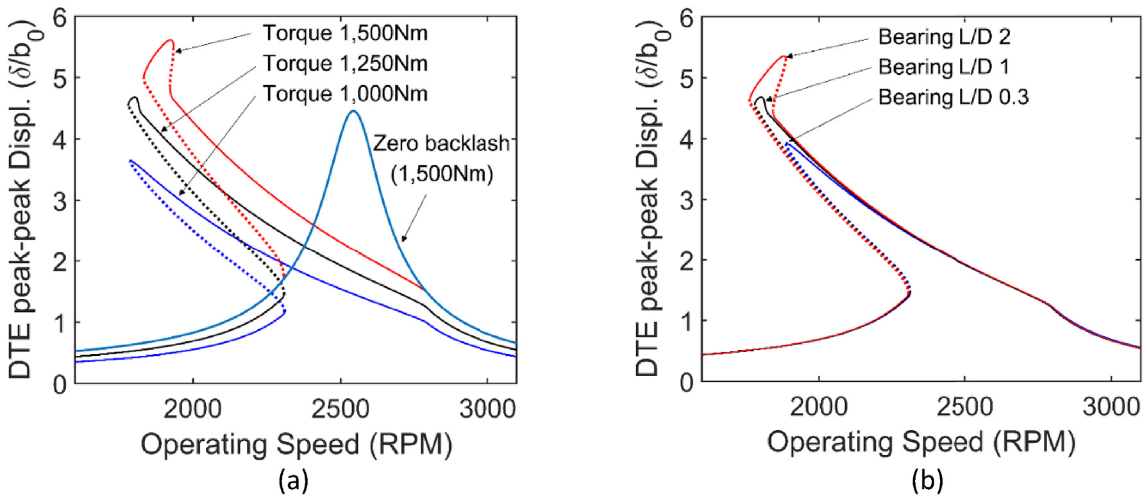

Fig. 8. Effect of (a) applied torque and (b) bearing L/D ratio on the peak-peak displacement of DTE through the fundamental resonance (solid line: stable, dotted line: unstable).

of $\frac{\omega_n}{N}$ where N represents the number of gear teeth. The presence of co-existing solutions is clearly seen to result from including backlash, and the peak DTE severity is seen to nearly double when backlash is included. Note that the time-varying stiffness effect is included in both the with and without backlash cases. The increased DTE caused by the gear nonlinearity is also confirmed by the time response of both cases at 2000 rpm in Fig. 7(b).

The results in Fig. 8 are obtained for three different applied torques T_1, i.e., 1,000, 1250 and 1500 N m ($T_2 = 0$), where T_1 is for driving gear and T_2 is for driven gear. All three cases exhibit a fundamental parametric resonance caused by the time-varying mesh stiffness, with a softening effect starting from near 2300 rpm. The amplitudes of the forced steady-state harmonic response increase with increased torque inputs. In all cases of Fig. 8(a), the unstable responses emerge through saddle-node bifurcations around 2300 rpm. Three or five multiple, co-existing steady-state responses occur between 1700 and 2300 rpm depending on the applied torque values. The critical rpm (2300 rpm) for jump-up behavior is nearly independent of applied torque variation, but in contrast, the critical rpm for jump-down behavior is more sensitive to applied torque variation. The critical rpm of jump-down behavior tends to increase with increasing drive torque. The separation between the jump-up and jump-down rpm is reduced with increasing applied torque. The emergence of the right-leaning portion of the response curves, which observed at the highest applied torque 1500 N m may be explained in terms of the backlash forces. Three different meshing states can exist depending on the maximum DTE; no impact, single-sided impact, and double-sided impact. In Fig. 8(a), the system shows only a single-sided contact with the 1000 N m applied torque, which is the source of the primary softening effect. Increasing the applied input torque gives rise to a hardening effect, which introduces additional co-existing responses and jump-up/down frequencies. The peak-peak response at 1500 N m shows a clear hardening effect along with the softening effect. The number of multiple co-existing responses increased from three to five with the applied torque increased from 1000 to 1500 N m. The figure also shows a tendency of the response curve to move rightwards towards the zero backlash response as the DTE increases. This is consistent with a greater engagement of teeth as the amplitude increases. These results are consistent with the experimental and numerical results in Ref. [4], which used a single-degree-of-freedom gear model considering only torsional motion. Prior research utilized a simple rigid or linear stiffness and damping bearing model, or analytical short bearing theory, or finite-length impedance method, which precluded the accurate investigation of nonlinear bearing parameter effects on the response. In this study, utilizing the finite element method for the nonlinear fluid film force of the finite-length bearing, the bearing L/D ratio is varied from 0.3 to 2 in Fig. 8(b). The peak-peak DTE displacements in the frequency range away from the resonance region are not significantly affected by the bearing L/D ratio variation. However, similar to the applied torque input case, the jump-down frequency is influenced by the L/D ratio variation, since the jump-down event occurs at a relatively lower frequency range with higher L/D ratio. The jump down speed is lowered by about 100 rpm for L/D = 2 compared with L/D = 0.3. Fig. 9 presents the bifurcation diagrams corresponding to the input torques 1000 and 1500 N m in Fig. 8(a), in a manner that highlights the jump phenomena and multiple co-existing solutions.

Fig. 10 illustrates the effect of varying bearing lubricant viscosity on steady-state, nonlinear harmonic response. Lubricant viscosities of 10 and 90 mPa s, in addition to the nominal value of 30 mPa s, are simulated for two L/D ratio (L/D = 0.3 and 1). Increasing the viscosity decreases the jump-down frequencies and increases the peak resonant amplitude in both L/D cases.

Fig. 11 shows the frequency-amplitude diagram with radial bearing clearances of $C_B = 184$ μm and $C_B = 74$ μm, along with nominal $C_B = 105$ μm. The results with the smallest clearance, i.e., $C_B = 74$ μm, show a broader range of co-existing solutions region compared to other values in both the L/D = 0.3 and the L/D = 1 cases. The $C_B = 74$ μm and L/D = 1 case displays a double-sided impact and resulting in hardening effect in Fig. 11(b). The L/D = 1 case shows more reduction in jump-down

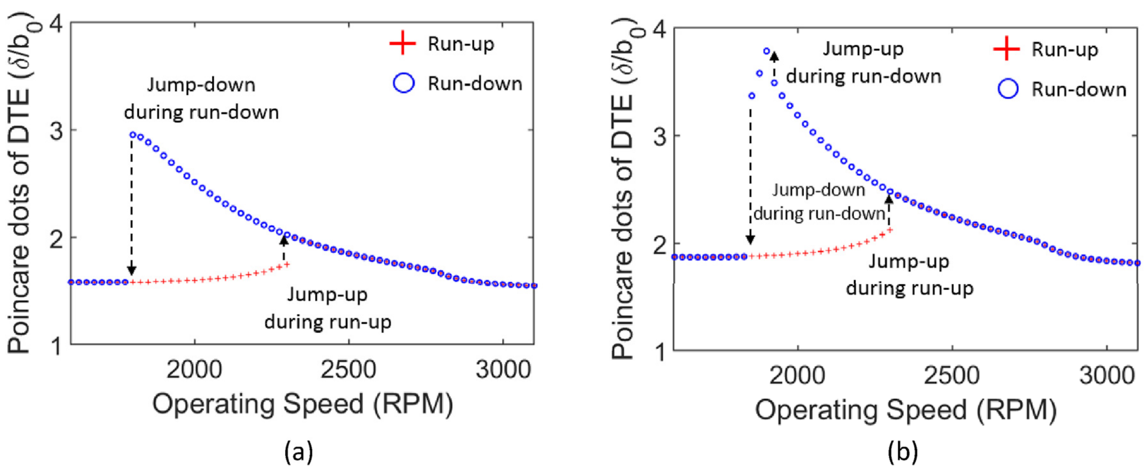

Fig. 9. Bifurcation diagrams of (a) 1000 N m torque and (b) 1500 N m torque cases in Fig. 8(a).

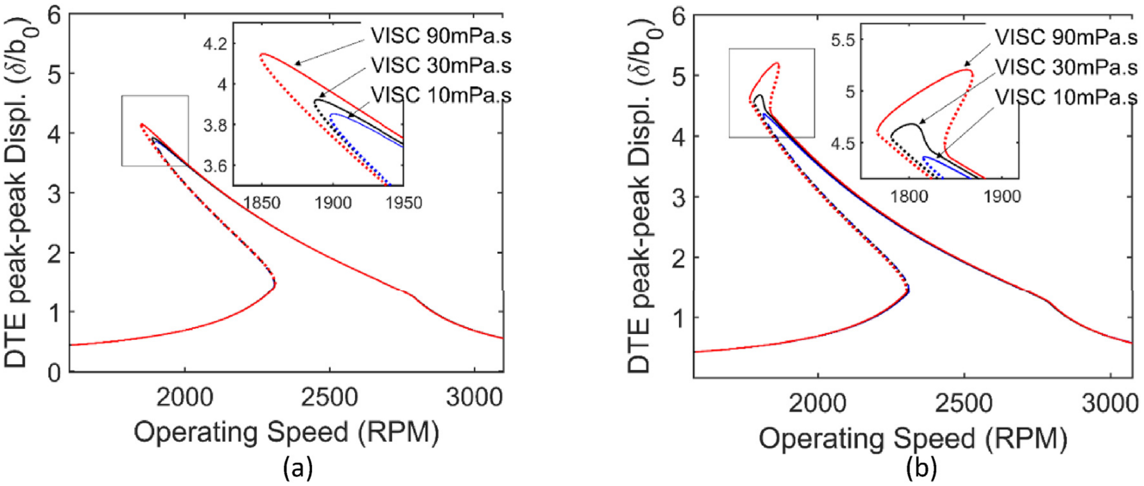

Fig. 10. Effect of lubricant viscosity on the peak-peak response of DTE (a) Bearing L/D = 0.3 and (b) Bearing L/D = 1 (solid line: stable, dotted line: unstable).

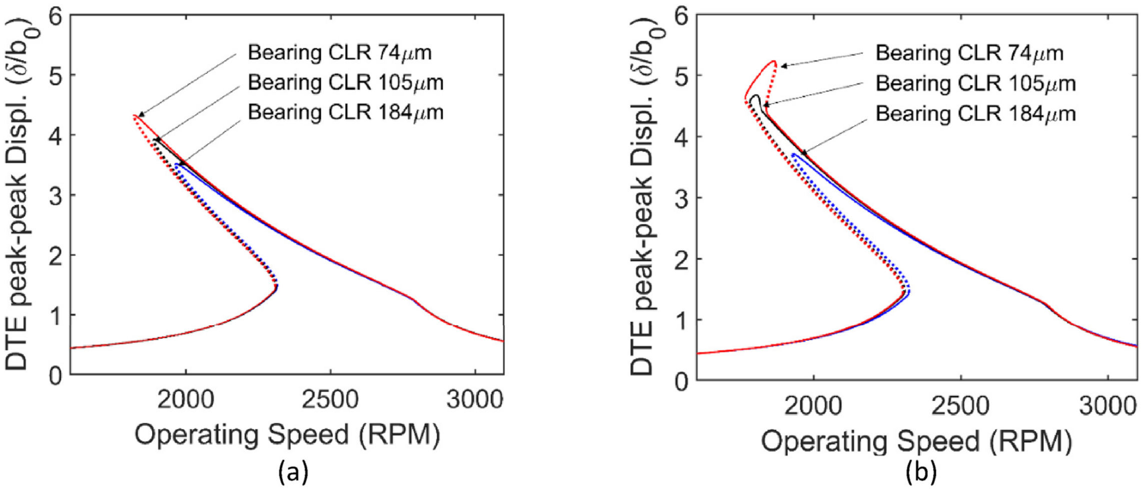

Fig. 11. Effect of bearing clearance on the peak-peak response of DTE (a) Bearing L/D = 0.3 and (b) Bearing L/D = 1 (solid line: stable, dotted line: unstable).

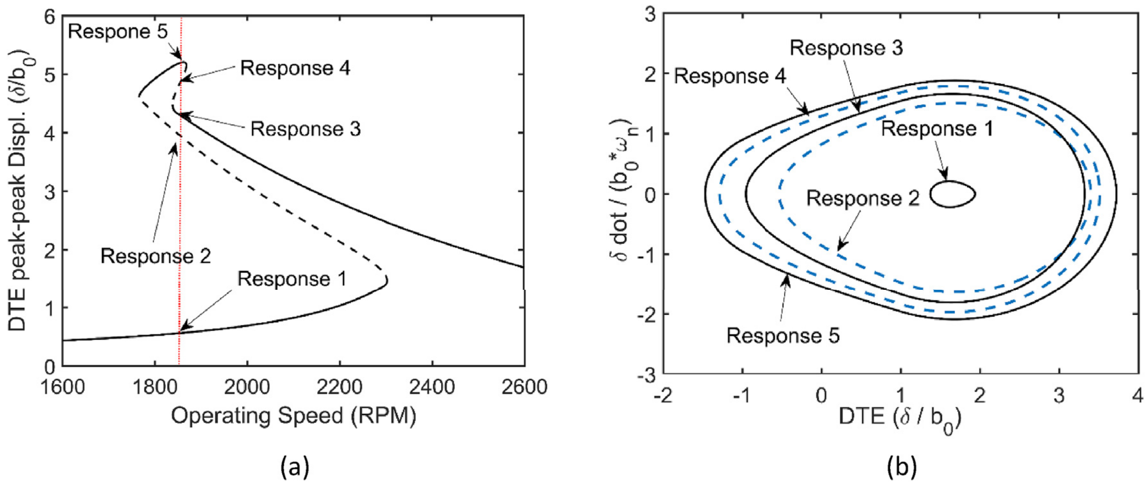

Fig. 12. Multiple co-existing responses using the shooting method (L/D = 1, μ = 90 mPa s, T_1 = 1500 N m). (a) Frequency-amplitude diagram (b) Phase portrait at 1850 rpm (Solid line: stable, dotted line: unstable).

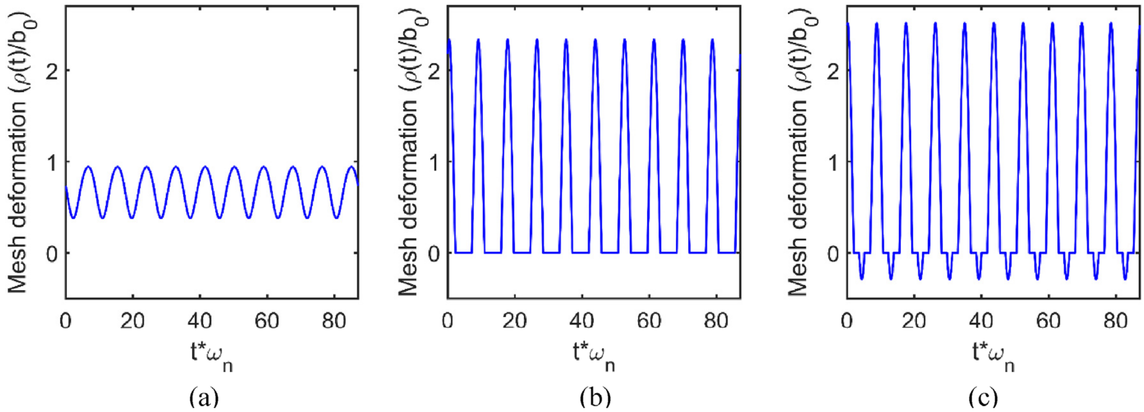

Fig. 13. Co-existing mesh deformation $\rho(t)$ responses: (a) Response 1 (b) Response 4 (c) Response 5.

frequency as compared to the L/D = 0.3 case. This reduction may be attributed to the fact that the L/D = 1 geometry has more fluid film area than for L/D = 0.3, and hence greater force to affect the parametric resonance.

Fig. 12 shows five co-existing steady-state responses in the frequency and phase plane domain for C_B = 74 μm case in Fig. 11 (b). For the phase portrait, the rotor spin speed equals 1850 rpm, and it is obtained via the non-autonomous MSM developed in section 3. The excitations include the time-varying mesh stiffness and the applied torque. Periodic responses 1, 3 and 5 are stable and 2 and 4 are unstable as predicted by the eigenvalues of the Jacobian matrix of the MSM. Note that the unstable forced harmonic responses cannot be obtained by direct numerical integration, but only with a directed search approach such as the MSM.

The mesh deformation $\rho(t)$ in Eq. (4) corresponding to the multiples responses in Fig. 12 are shown in Fig. 13. The mesh deformation in Fig. 13(a) has static and dynamic components and never loses contact. The response in Fig. 13(b) has zero mesh deformation for most of the period and demonstrates the effect of single-sided contact induced by the backlash nonlinearity. Fig. 13(c) shows double-sided contact cycling between positive, zero and negative mesh deformation states. The result of this contact behavior is a net hardening effect as evidenced by the right-leaning secondary bend in the response 5 curve of Fig. 12.

Fig. 14 illustrates the repelling/attracting motions among stable and unstable forced harmonic response orbits at 1850 rpm. The unstable Response 2 is repelled towards the stable attractors, i.e. Response 1 (Fig. 14(a)) or Response 3 (Fig. 14(b)). Thus, the unstable manifold (the dotted line) initiated by a saddle-node bifurcation in Fig. 12 acts as a border manifold, which provides information about the convergence route in phase space.

4.1.2. Subharmonic resonances

Prior work [3,38,39] revealed that subharmonic resonance of geared systems is highly dependent on the amplitude of time-varying mesh stiffness, mesh damping ratio and static applied torque. The focus here is to demonstrate the effect of journal bearing parameters on the subharmonic vibrations occurring for a rotor speed in the vicinity of $\frac{2\omega_n}{N}$. The maximum

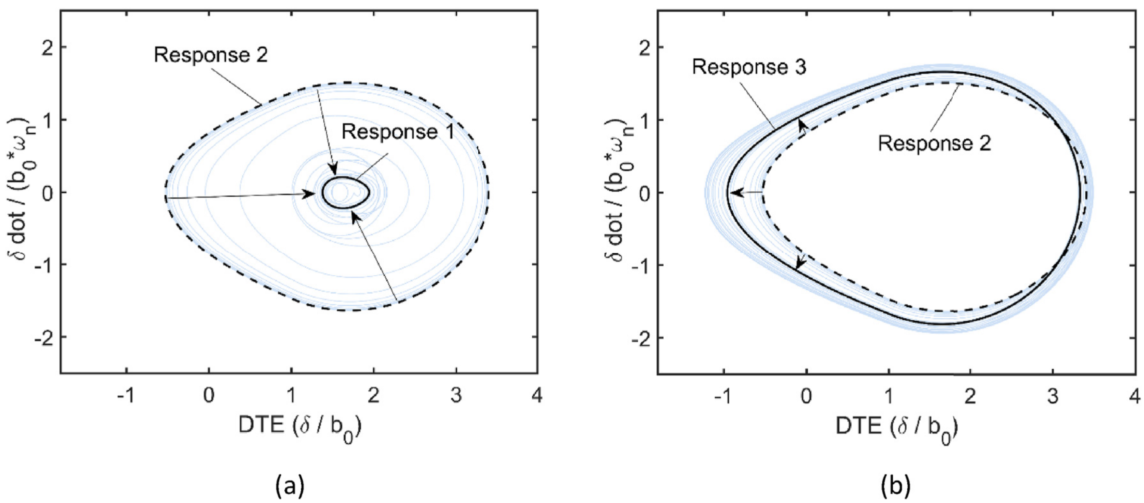

Fig. 14. Repelling motion of the unstable orbit (response 2) at fundamental resonance region (a) Response 2 → Response 1 (b) Response 2 → Response 3 (solid line: stable, dotted line: unstable).

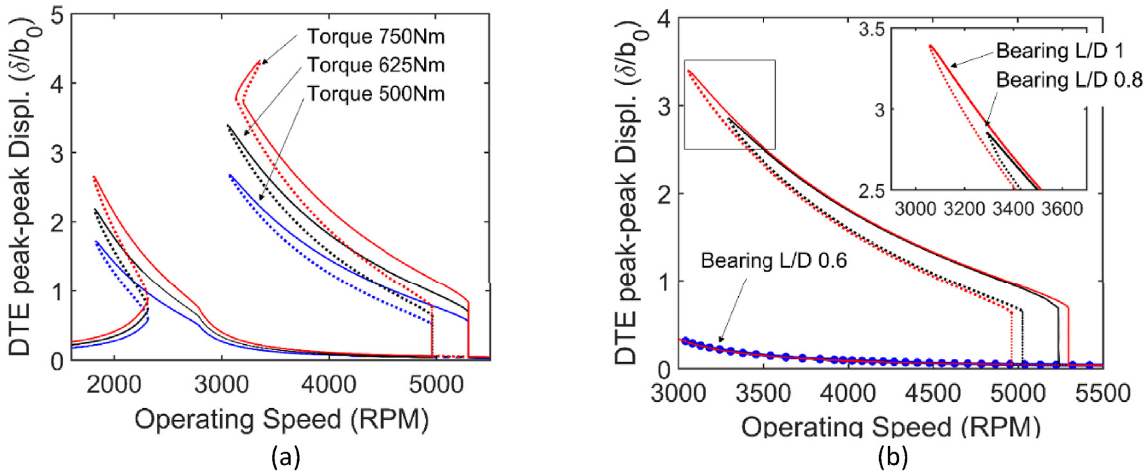

Fig. 15. Effect of (a) applied torque and (b) bearing L/D ratio on the peak-peak response of DTE of subharmonic resonance (solid line: stable, dotted line: unstable).

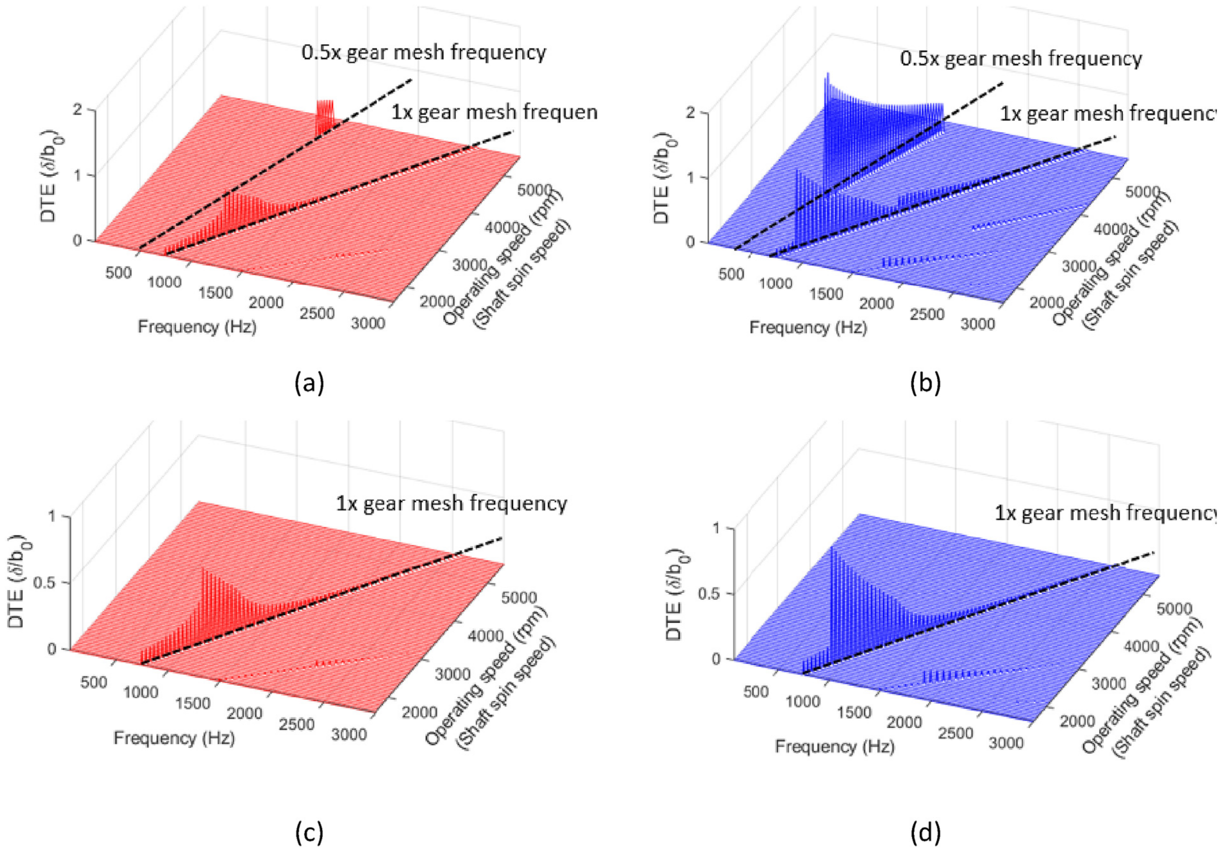

Fig. 16. Waterfall diagrams (a) 750 N m Torque, run-up, (b) 750 N m Torque, run-down, (c) L/D = 0.6, run-up, (d) L/D = 0.6, run-down.

rpm is extended from 3100 rpm for the fundamental resonance case to 5500 rpm to observe the subharmonic resonances. Fig. 15(a) shows that increasing torque increases the peak-peak DTE amplitude, the backlash nonlinearity generally causes a softening (left-leaning resonance) effect, but a double-sided contact is evidenced by the right-leaning, hardening peak at 750 N m torque, similar with the fundamental resonance in Fig. 8.

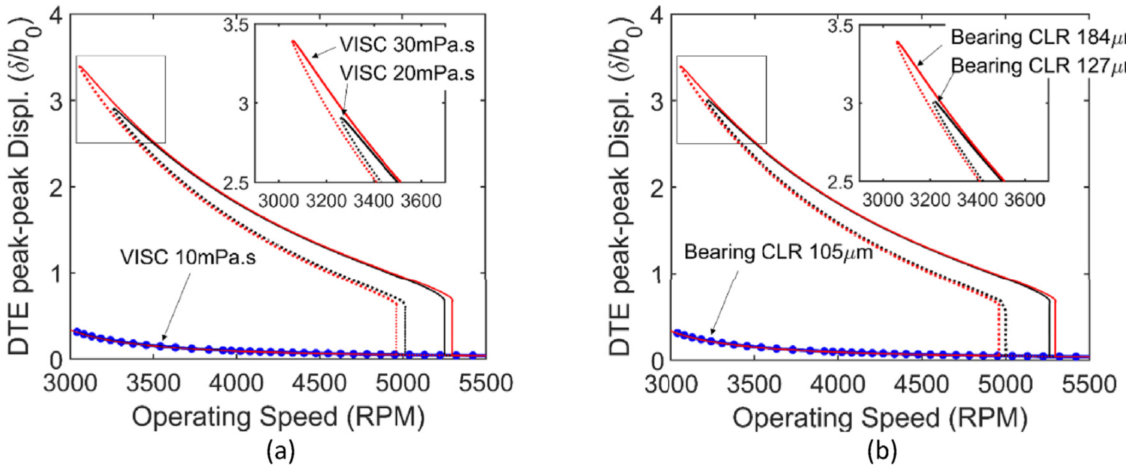

Fig. 17. Effect of (a) lubricant viscosity and (b) bearing clearance on the peak-peak response of DTE for subharmonic resonance (solid line: stable, dotted line: unstable).

Fig. 16 provides waterfall diagrams corresponding to the 750 N m torque case in Fig. 15(a) and the bearing L/D = 0.6 case in Fig. 15(b). Fig. 16(a) and (b) correspond to run-up and run-down in speed for the 750 N m torque case with L/D = 1. Fig. 16(c) and (d) correspond to run-up and run-down in speed for the bearing L/D = 0.6 case with 625 N m torque input. The figures show jump-up and jump-down bifurcations near 2500 rpm, and the presence of a sub-harmonic resonance and a 0.5x gear mesh frequency response.

In Fig. 15, unstable branches appear as a period-doubling bifurcation emerges near 5000 rpm, which corresponds to twice the fundamental resonance frequency rotor speed ($\frac{2\omega_n}{N}$). A saddle-node bifurcation occurs as the period-doubled unstable branches reach their peak amplitude, yielding a stable branch. As a result, one stable solution with the gear mesh frequency (ω_g) and two unstable/stable solutions with half gear mesh frequency ($0.5\omega_g$) coexist in the operating speed range between 3000 and 5000 rpm.

Variation of the journal bearing parameters significantly affects the subharmonic resonance as shown in Figs. 15(b) and 17. The sub-harmonic resonance is seen to vanish when considering a drop in L/D from 0.8 to 0.6. Physically this may result from the more significant force of the larger L/D bearing inducing the subharmonic vibrations. Fig. 17(a) shows that increasing the lubricant viscosity extends the frequency overlap range by decreasing the jump-down frequency. Similar trends are also observed in the case of bearing clearance in Fig. 17(b). The subharmonic is seen to disappear for the low viscosity (10 mPa s) case and the low clearance (105 μm) case. Fig. 18 shows multiple co-existing DTE versus time plots for the 30 mPa s case in Fig. 17(a): 3575 rpm, L/D = 1, an applied torque of 625 N m, a lubricant viscosity of 30 mPa s and a bearing clearance of 36.8 μm. The $t\omega_n$ in Fig. 18 is the non-dimensional time variable where the time t is multiplied by the torsional natural frequency ω_n. Note that the Response 1 in Fig. 18 (a) has the frequency equal to ω_g, while the Response 2 and 3 in Fig. 18(b) and (c) have the half frequency of ω_g.

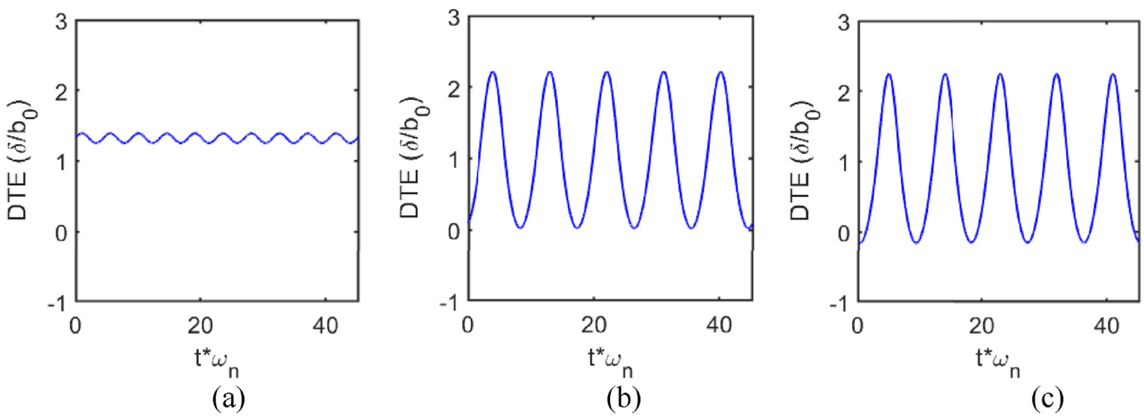

Fig. 18. Time response of multiple co-existing response of DTE (a) Response 1, (b) Response 2, (c) Response 3.

4.2. Chaotic response

The effect of linearized bearing model stiffness and damping coefficients, static transmission error, tooth friction, etc. on the chaotic response of geared systems was investigated in Refs. [2,6,7,24,40,41], and chaotic behavior was observed experimentally in Ref. [6]. The effects of varying journal bearing parameters using a nonlinear bearing model, on the geared system's chaotic response are discussed below. The model parameter values include a low torque load of 200 N m, a light mesh damping ratio of 0.01, L/D = 0.3, and the mean static transmission error e_0 is set to b_0, the coefficient of static transmission error p_j in Eq. (2) is set to 0.15. Unbalance force is not included in this simulation. The nonlinear equations are solved using MATLAB's ODE 15s with a relative tolerance of 10^{-5}. The time response corresponding to the first 1500 gear mesh periods of the system was discarded from the sampled data to ensure that the responses reached steady-state conditions. The steady-state responses during the last 500 gear mesh periods were employed for the plots shown below. The MLEs of the spur gear system were plotted to identify the onset of chaotic motion. The MLEs converged after 600-time intervals with 0.25 gear mesh periods per interval.

Fig. 19 shows DTE bifurcation diagrams versus rotor rpm while varying torque, bearing lubricant viscosity and radial clearance. The viscosity and clearance are held fixed at 40 mPa s and 105 μm, respectively, while varying torque in Fig. 19(a). The torque and clearance are held fixed at 1100 N m and 105 μm respectively while varying viscosity in Fig. 19(b). The torque

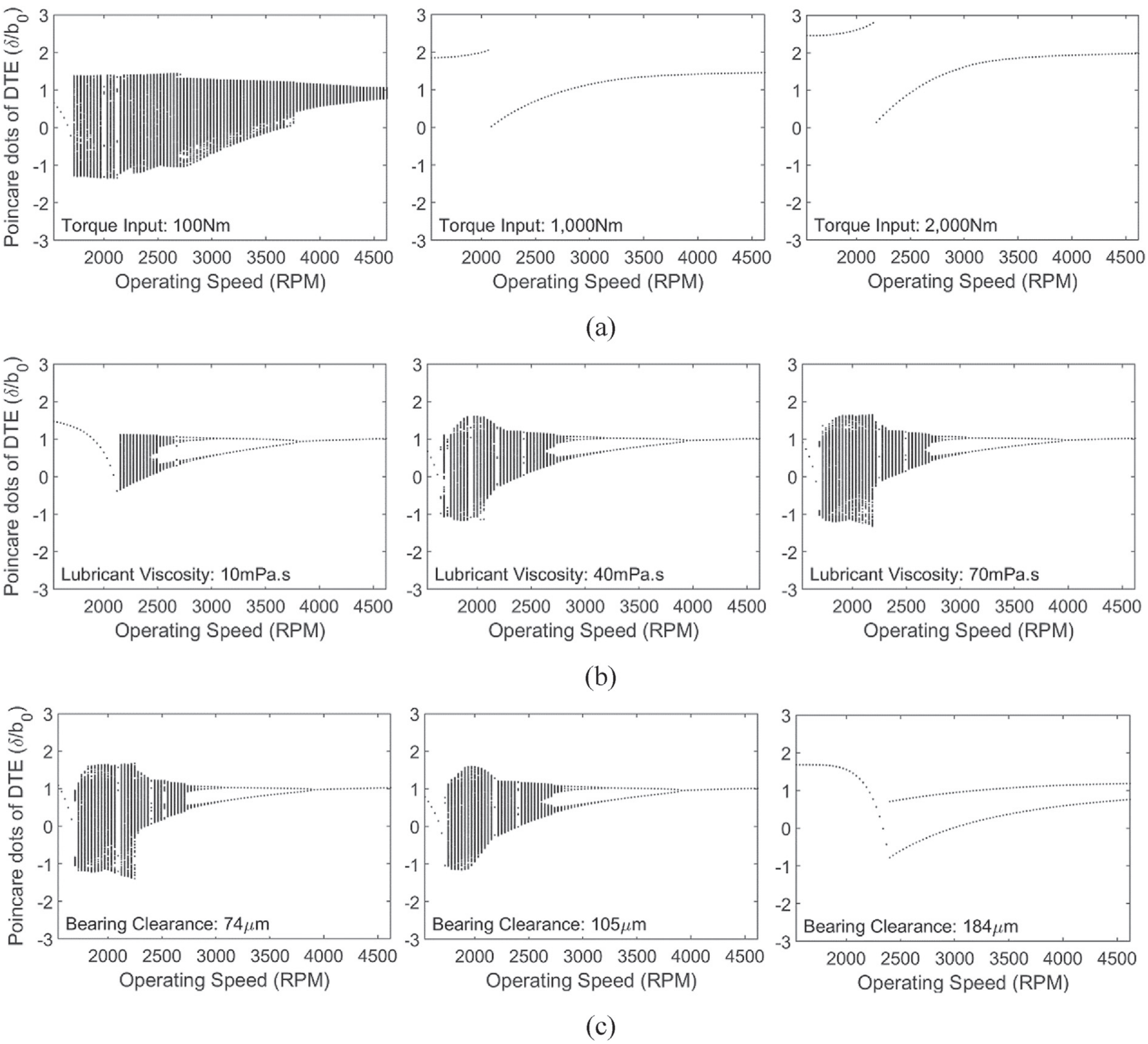

Fig. 19. Bifurcation diagrams vs. operating speed for varying parameter values (a) applied torque (100, 1000 and 2000 N m) (b) lubricant viscosity (10, 40 and 70 mPa s), and (c) Bearing clearance (74, 105 and 184 μm).

and viscosity are held fixed at 1100 N m and 40 mPa s respectively while varying radial clearance in Fig. 19(c). The Poincaré dots are sampled at the gear mesh frequency period ($\Delta t = \frac{2\pi}{\omega_g}$).

With a relatively low applied torque (100 N m), the system performs 1× synchronous motions at the gear mesh frequency until the operating speed reaches about 1800 rpm. Then chaotic responses emerge and are maintained at higher speeds. Note that with increasing applied torque from 1000 to 2000 N m, the operating speeds where jump occurs are slightly increased from 2050 to 2150 rpm, which implies that the variation of applied torque has an impact on the natural frequencies of the geared system supported by journal bearings, via a torsional-lateral coupling. Comparison of three cases reveals that the increasing torques tend to mitigate the chaotic responses.

Fig. 19(b) shows that the chaos in DTE response starts at lower speed and ranges over a larger set of values as the bearing lubricant viscosity increase from 10 to 70 mPa s. In all three diagrams of Fig. 19(b), with higher operating speeds over 2500 rpm, the chaotic responses turn into period four and two motions, and eventually into period one motion. Fig. 19(c) shows how the chaotic behavior in DTE occurs with the radial bearing clearance values from 74 to 184 μm. Period-doubling bifurcations occur with decreasing speeds from 4500 rpm to lower speeds in the 74 and 105 μm cases, as exemplified by the period one motion turning into period two motion around 3800 rpm, followed by additional period doubling into chaos. In Fig. 19(b) and (c), the lower viscosity and high bearing radial clearance tend to suppress the chaotic behaviors and show relatively stable motions.

Fig. 20 is included to more clearly illustrate the occurrence of chaotic and period-doubling bifurcations corresponding to the 40 mPa s case in Fig. 19(b). Attractors are presented for the four different operating speeds (2300 rpm, 2900 rpm, 3500 rpm and 4100 rpm). The strange attractor and corresponding positive MLE value of 0.056 both confirm chaotic behavior at 2300 rpm. The number of attractors (4 → 2→1) confirms the occurrence of period-doubling bifurcations as the speed decreases from 4100 to 3500 to 2900 rpm.

Fig. 21 shows DTE bifurcation and MLE diagrams versus applied torque, journal bearing radial clearance and viscosity, at the fixed operating speed 1540 rpm. The viscosity is held fixed at 30 mPa s, and the clearance is held fixed at 100 μm while varying torque in Fig. 21(a). The Fourier coefficient of the static transmission error in Eq. (2) is set to 0.15 and applied to the system. The sampling frequency of Poincaré dots is the gear mesh frequency ω_g.

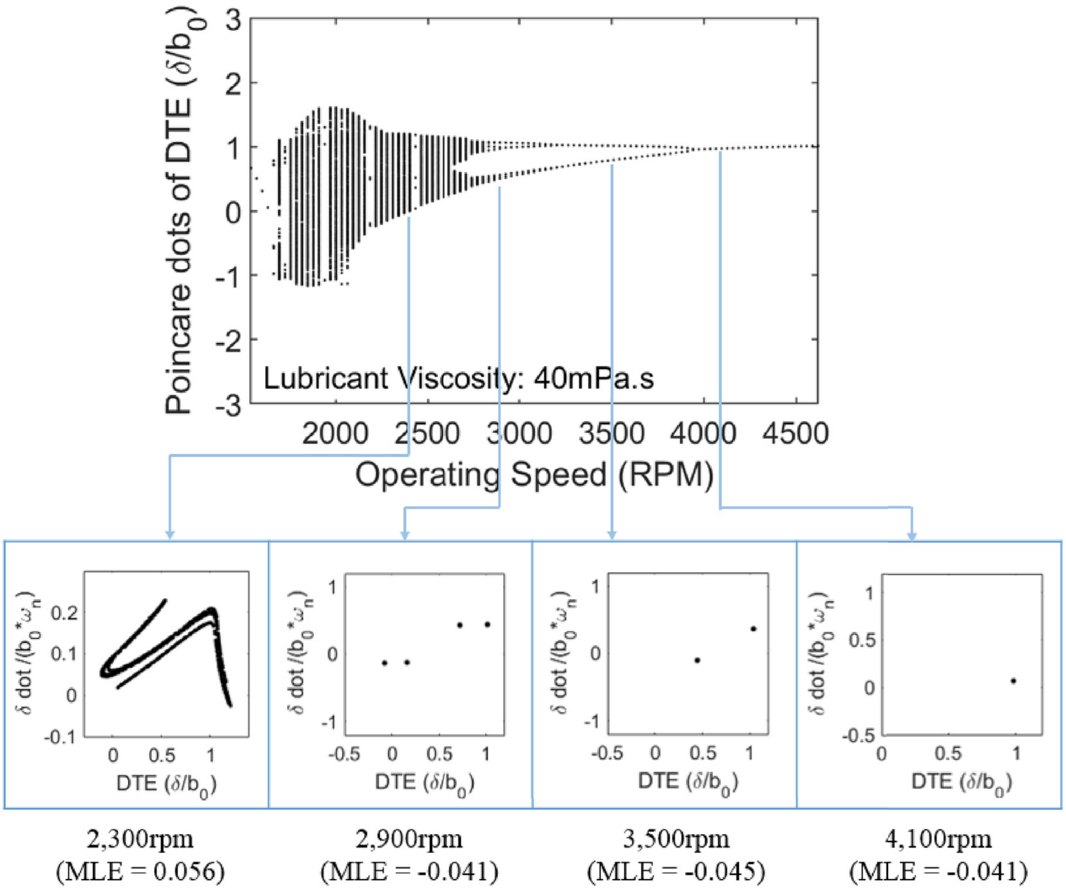

Fig. 20. Bifurcation diagrams and Poincaré attractors at different speeds, for a lubricant viscosity 40 mPa s case in Fig. 19(b).

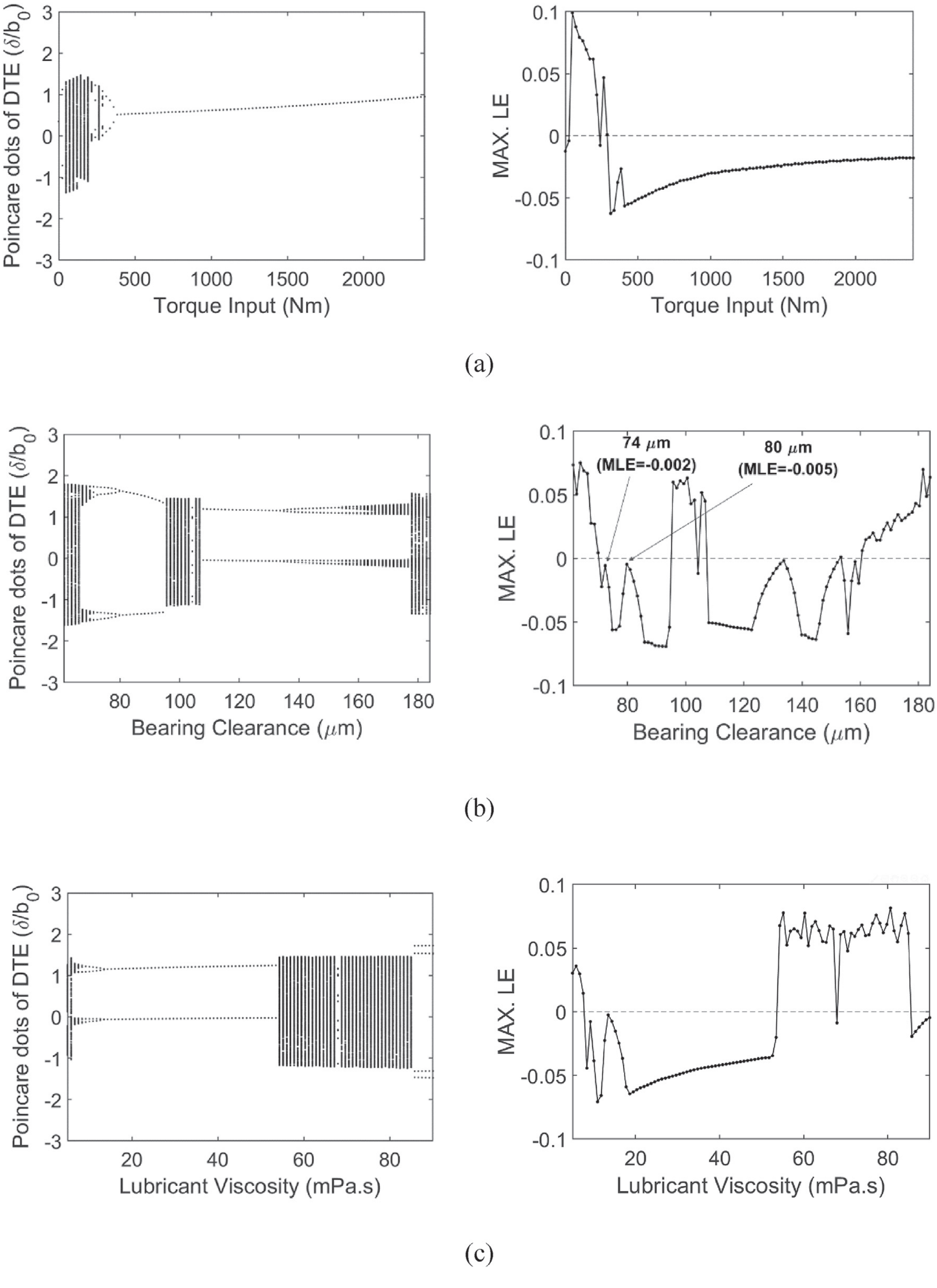

Fig. 21. Bifurcation and MLE diagrams vs. (a) applied torque (0–2400 N m), (b) bearing clearance (60–185 μm) and (c) lubricant viscosity (5–90 mPa s).

The MLEs quantitatively confirm the existence of chaotic behavior. Fig. 21(a) presents the bifurcation diagram and MLE plot with applied torque ranging from 0 to 2400 N m. Increasing the applied torque is seen to eliminate chaotic motion, and synchronous 1× motion appears at applied torques above 400 N m. The MLEs show positive values, indicating chaos, with low applied torque (<400 N m). For instance, at 200 N m, the corresponding MLE has the positive value of +0.07.

The radial bearing clearance is varied from 60 to 185 μm in Fig. 21(b) with the rotor speed at 1540 rpm and the lubricant viscosity of 30 mPa s. Chaotic motion occurs in three separate clearance ranges (i.e., 60–70 μm, 95–105 μm, 175–185 μm), and period-doubling routes to chaos with decreasing and increasing parameter values are observed in the ranges 60–80 μm and 130–180 μm, respectively. In Fig. 21(c), the applied torque is held fixed at 100 N m, and the clearance is held fixed at 100 μm

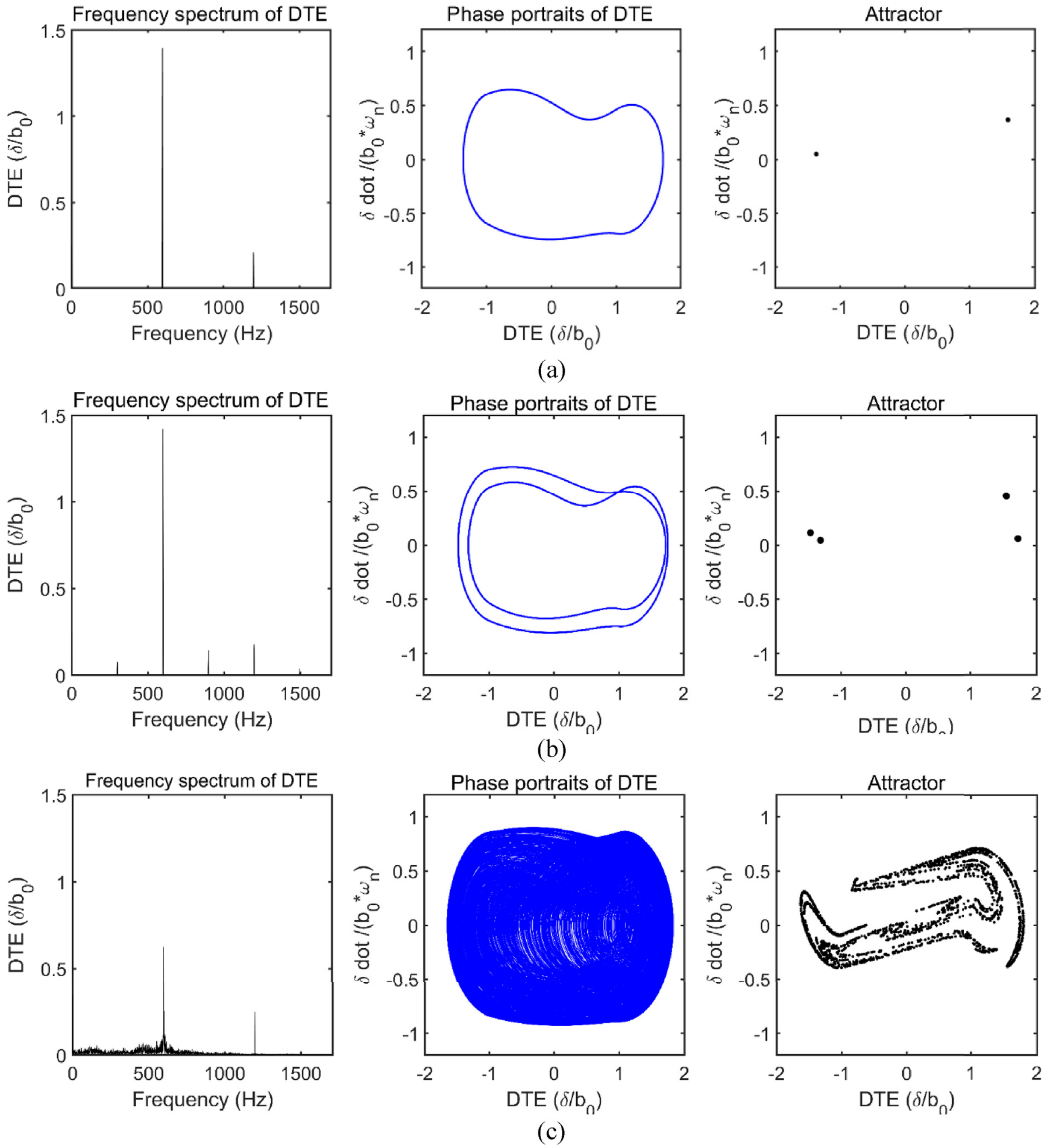

Fig. 22. Frequency spectra, phase portraits and Poincaré attractors of dynamic transmission error (DTE) for different bearing clearances (a) 80 μm (b) 74 μm (c) 61 μm in Fig. 21(b).

while varying viscosity. The figure shows chaos appearing in two ranges of lubricant viscosity: over the ranges of 0–7 mPa s and 55–85 mPa s. All bifurcation diagrams in Fig. 21 display the period-doubling route to chaos, which indicates that the system goes into chaotic states by doubling its period with increasing or decreasing control parameters.

The periodic, period-doubling and chaotic DTE behaviors implied in Fig. 21(b) for bearing clearance variation, are further confirmed in the frequency spectrum, phase portrait, and Poincaré attractor plots in Fig. 22. Three radial bearing clearance values, i.e., 80, 74 and 61 μm, are examined. As can be seen by comparing Figs. 21(b) and 22(a) and (b), the geared system with MLE $= -0.005$ (80 μm case) and -0.002 (74 μm case) has period two and period four DTE responses, respectively, confirmed by the Poincaré attractors. The 61 μm bearing clearance case in Fig. 22(c) was selected to illustrate chaotic DTE response based on an MLE (+0.06), from Fig. 21(b). The phase portrait orbit has a clear aperiodic response, the frequency spectrum has a broadband character, and the corresponding Poincaré dots form a strange attractor. These results show that the system experiences period-doubling bifurcation with decreasing bearing clearance as the system transitions into chaotic responses.

4.3. Effect of gear mesh stiffness on oil whirl

Oil whirl is a rotor dynamics term describing a self-excited, shaft vibration anomaly common to rotating machinery supported by oil film, fixed pad, journal bearings. The dominant symptom of oil whirl is a sub-synchronous limit cycle vibration that is sustained by the journal bearing forces, as opposed to the external excitation such as rotor mass imbalance. In this section, the effect of gear mesh stiffness on the oil whirl instability is investigated. The bearing supported geared rotor pair is modeled as an autonomous (unforced) system with perfectly balanced rotors, and as such is analyzed utilizing the autonomous shooting method. The multiple shooting/continuation method for autonomous cases developed in section 3 is used for identifying periodic solutions. This approach for drawing the bifurcation diagrams was incapable of finding the solutions near saddle-node bifurcations without manual assistance. The continuation algorithm was restarted near the saddle-node bifurcation points and the step size was reduced to help the solutions converge. This typically requires two or three restarts to plot one complete bifurcation diagram.

Fig. 23 shows a bifurcation diagram of the non-dimensional maximum and minimum vertical position of the rotor center in the load direction versus operating speed. Results are shown for two mesh stiffness values, i.e., $k_0 = 1e7$ N/m and 1e9 N/m. The input torque applied to the gear pair is 1000 N m. Run-up/run-down simulations are conducted separately, using direct numerical integration, and the two results are combined to generate the figure. In Fig. 23(a), as the operating speed increases, the jump-up phenomenon is observed at 37,500 rpm, which corresponds to the onset speed of oil whirl. Jump-down frequency is also predicted at 34,500 rpm with run-down simulation, and consequently, the amplitude of vertical rotor response has been abruptly reduced at the same speed. The result with high mesh stiffness value, i.e., 1e9 N/m in Fig. 23(b), shows a delayed onset speed of oil whirl compared with 1e7 N/m case, such that the jump-up and jump-down frequencies are predicted at 39,500 and 37,000 rpm, respectively. From this result, it is verified that mesh stiffness variation not only affects the high frequency vibration in a geared system but also may change the characteristics of hydrodynamic stability of a geared system supported by journal bearings.

It should be noted that the result with direct numerical integration is incapable of identifying co-existing solutions and the stability of responses. The bifurcation diagram is obtained with the continuation algorithm and the result is presented in

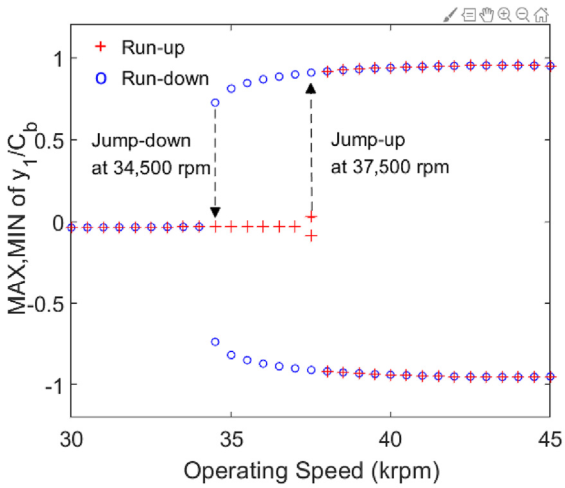

(a)

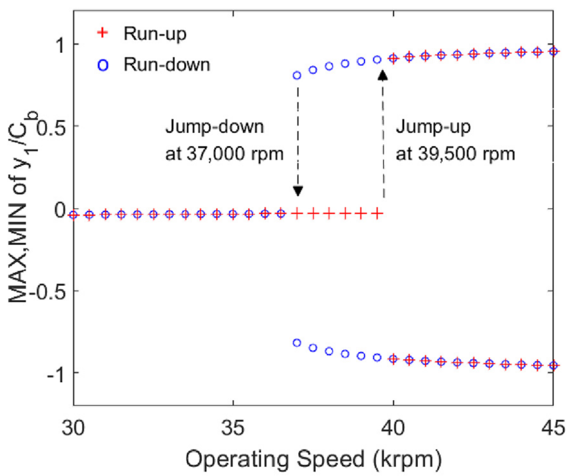

(b)

Fig. 23. Run-up and run-down simulations using direct numerical integration (a) mesh stiffness 1e7 N/m (b) mesh stiffness 1e9 N/m.

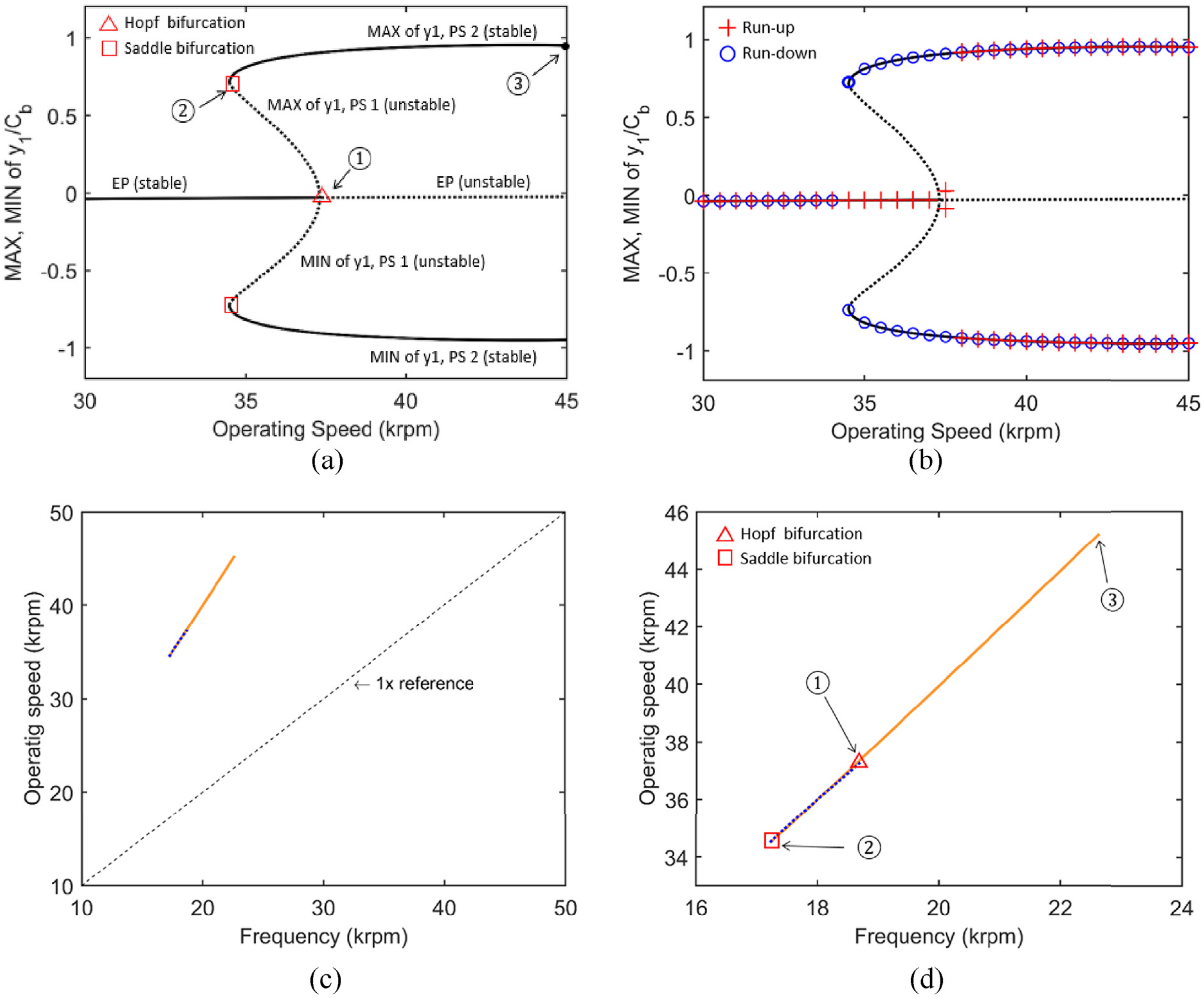

Fig. 24. Bifurcation diagram using shooting/continuation method with mesh stiffness 1e7 N/m and applied torque 1000 N m: (a) Bifurcation diagram using continuation algorithm, (b) result from continuation algorithm compared with numerical integration, (c) revolution speed versus response frequency and (d) zoom of (c).

Fig. 24. In the case of mesh stiffness 1e7 N/m, in Fig. 24(a), the stable equilibrium position EP which is maintained over low operating speeds switches to unstable motion after crossing Hopf bifurcation point at 37,210 rpm. The transition from stable to unstable response is verified with the continuation algorithm, which provides the eigenvalues of the Jacobian matrix moving out of the unit circle in the complex plane. The point ① corresponds to a Hopf bifurcation, where an unstable subsynchronous response PS 1 emerges and approaches the saddle bifurcation point ②. The amplitudes of the maximum and minimum responses of PS 1 quickly grow as the speed decreases until the saddle point is reached. After the saddle bifurcation, the subsynchronous branch becomes the stable response PS 2 and its maximum and minimum amplitudes slowly approach the bearing clearance limit. The results using the continuation algorithm are drawn in the same figure with the direct numerical integration results in Fig. 24(b). Two results agree well throughout the all speed ranges, except the unstable subsynchronous response PS 1 is only predicted with the continuation algorithm. The vibration frequencies of the branches are shown in Fig. 24(c) and its zoomed version in (d). The frequency range where subsynchronous vibration was observed is located between 17,000 and 23,000 rpm, which corresponds to the 45−50% of operating speed.

Bifurcation diagrams with three different mesh stiffness (1e7, 1e8 and 1e9 N/m) at 1000 N m torque are drawn using the continuation algorithm in Fig. 25. The onset speed of oil whirl is increased from 37,210 to 39,310 rpm as the mesh stiffness increases from 1e7 to 1e8 N/m. In contrast, the onset speed shift is relatively insignificant (110 rpm) between higher mesh stiffness cases, i.e., 1e8 and 1e9 N/m. This result shows that the gear and the journal bearing parameters are coupled and the variation of gear parameter may affect the hydrodynamic stability characteristics of fluid film bearings.

The effect of applied torque on oil whirl onset speed was presented in Refs. [30,33], and the results showed that higher applied torque on the geared system delayed the oil whirl onset speed. This aspect of applied torque effect on oil whirl onset

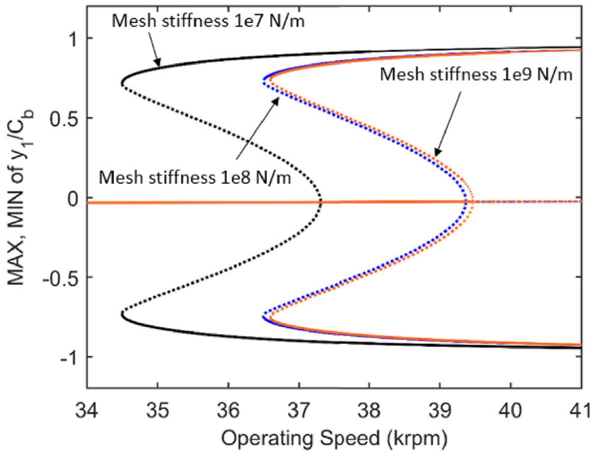

Fig. 25. Bifurcation diagrams with various mesh stiffness values (1e7, 1e8 and 1e9 N/m) and with an applied torque of 1000 N m.

Table 3
Oil whirl onset speed with different torque and mesh stiffness (Identified utilizing Continuation algorithm).

Applied torque	1e7 N/m	1e8 N/m	1e9 N/m	Onset speed difference
50 N m	10,450 rpm	10,480 rpm	10,490 rpm	40 rpm
200 N m	18,760 rpm	18,890 rpm	18,910 rpm	150 rpm
400 N m	25,360 rpm	25,780 rpm	25,800 rpm	440 rpm
600 N m	30,750 rpm	31,390 rpm	31,410 rpm	660 rpm
800 N m	34,780 rpm	36,070 rpm	36,130 rpm	1350 rpm
1000 N m	37,210 rpm	39,310 rpm	39,420 rpm	2210 rpm

speed may be affected by the amplitude of gear mesh stiffness. The interaction between the applied torque and gear mesh stiffness is investigated with various torque and mesh stiffness values in Table 3. Six applied torque amplitudes from 50 to 1000 N m were applied as mesh stiffness varies from 1e7 to 1e9 N/m. The onset speed of oil whirl is identified by employing the continuation algorithm to find the speed where the jump-up phenomenon occurs. As observed in the reference [30,33], the onset speed generally increases with higher applied torques for all three stiffness cases. From the table, it is also evident that the effect of mesh stiffness magnitude on the onset speed is closely related to the amplitude of torque values. When the lowest applied torque (50 N m) is applied, the onset speed delay caused by the mesh stiffness variation from 1e7 to 1e9 N/m is only 40 rpm. Meanwhile, the speed delay increases up to 2210 rpm with the application of the highest torque value (1000 N m). This result confirms that the transition of oil whirl onset speed with different mesh stiffness is less significant at lower applied torques.

5. Conclusions

The nonlinear behavior and bifurcation of a geared rotor system supported by fluid film journal bearings were investigated employing a multiple shooting/continuation algorithm. Nonlinear effects included in the model are nonlinear fluid film force in journal bearing, gear backlash, and time-varying mesh stiffness. The present study confirms that the nonlinearities in a gear pair may induce nonlinear behaviors such as the jump phenomenon, co-existing responses, subharmonic resonances and chaotic responses in the five-degree-of-freedom, gear-journal bearing system model.

The effect of the gear applied torque and journal bearing paramaters on the nonlinear phenomena were investigated. The simulation with varying gear input torque showed that the separation between jump-up and jump-down speed is reduced with high input torques. The high input torque also induced a hardening effect which is not observed in low torque values. It was also confirmed that as bearing L/D ratio and bearing lubricant viscosity are increased, or bearing clearances are decreased, the frequency where the gear nonlinearity-induced jump phenomenon occurs is lowered, and the number of multiple responses is increased, along with the double-sided contact of meshes. In addition, the influence of the input torque and journal bearing parameters on the subharmonic responses were investigated. The simulation results revealed that the high input torque gives rise to the hardening effect as well as the softening effect in the subharmonic resonance region. It is also shown that small bearing L/D ratio, lubricant viscosity and bearing clearance suppress the subharmonic resonances.

The impact of journal bearing parameters on the chaotic response were investigated via direct numerical integration, bifurcation diagrams, spectrums, Poincaré attractors and maximum Lyapunov exponents. As compared to the former studies, which used the linearized bearing stiffness and damping coefficients, the present study utilized the nonlinear journal bearing modeled with the finite element method. The results showed that the high-applied input torques to the gear suppress the chaotic response in the system. Chaotic motions and period-doubling bifurcations were observed at constant operating speed, as the value of lubricant viscosity and bearing clearance varied.

The effect of gear mesh stiffness on the oil whirl phenomenon of the journal bearing was also studied. Using the continuation algorithm, it was verified that the increased gear mesh stiffness delays the onset speed of oil whirl. In addition, the mesh stiffness effect on the oil whirl phenomenon was sensitive to the magnitude of the gear input torque, as the amount of the onset speed delay was found to be more significant with high input torques.

Future investigations for bifurcation and nonlinear dynamics of a gear supported by journal bearings will include thermal effect in the bearing lubricant, other types of hydrodynamic journal bearings such as pressure dam or tilting pad bearings. A more detailed gear-rotor model including a finite element shaft and a lubricant between gear meshes will also be developed. Experimental verification will be conducted to obtain validation results for the theoretical models.

Declaration of competing interest

The authors declare that they have no known competing financial interests or personal relationships that could have appeared to influence the work reported in this paper.

CRediT authorship contribution statement

Dongil Shin: Investigation, Visualization, Writing - original draft, Data curation, Software, Methodology, Conceptualization. **Alan Palazzolo:** Methodology, Supervision, Validation, Writing - review & editing.

Acknowledgment

The authors gratefully acknowledge the financial support on this research from the Texas A&M Turbomachinery Research Consortium (TRC).

References

[1] A. Kahraman, R. Singh, Non-linear dynamics of a spur gear pair, J. Sound Vib. (1990), https://doi.org/10.1016/0022-460X(90)90582-K.
[2] A. Kahraman, R. Singh, Non-linear dynamics of a geared rotor-bearing system with multiple clearances, J. Sound Vib. (1991) 469–506.
[3] A. Kahraman, R. Singh, Interactions between time-varying mesh stiffness and clearance non-linearities in a geared system, J. Sound Vib. (1991), https://doi.org/10.1016/0022-460X(91)90527-Q.
[4] G.W. Blankenship, A. Kahraman, Steady state forced response of a mechanical oscillator with combined parametric excitation and clearance type nonlinearity, J. Sound Vib. 185 (1995) 743–765.
[5] A. Kahraman, G.W. Blankenship, Interactions between commensurate parametric and forcing excitations in a system with clearance, J. Sound Vib. (1996), https://doi.org/10.1006/jsvi.1996.0361.
[6] A. Kahraman, G.W. Blankenship, Experiments on nonlinear dynamic behavior of an oscillator with clearance and periodically time-varying parameters, J. Appl. Mech. 64 (1997) 217, https://doi.org/10.1115/1.2787276.
[7] A. Raghothama, S. Narayanan, Bifurcation and chaos in geared rotor bearing system by incremental harmonic balance method, J. Sound Vib. (1999), https://doi.org/10.1006/jsvi.1999.2264.
[8] S. Natsiavas Theodossiades, Non-linear dynamics of gear-pair systems with periodic stiffness and backlash, J. Sound Vib. (2000), https://doi.org/10.1006/jsvi.1999.2490.
[9] A. Al-Shyyab, A. Kahraman, Non-linear dynamic analysis of a multi-mesh gear train using multi-term harmonic balance method: period-one motions, J. Sound Vib. 284 (1–2) (2005) 151–172.
[10] A. Al-Shyyab, A. Kahraman, Non-linear dynamic analysis of a multi-mesh gear train using multi-term harmonic balance method: sub-harmonic motions, J. Sound Vib. 279 (1–2) (2005) 417–451.
[11] S. Zhou, J. Liu, C. Li, B. Wen, Nonlinear behavior of a spur gear pair transmission system with backlash, J. Vibroeng. 16 (2014) (1465) 3850–3861.
[12] Y. Yang, H. Li, Y. Dai, Nonlinear vibration characteristics of spur gear system subjected to multiple harmonic excitations, Proc. Inst. Mech. Eng. Part C J. Mech. Eng. Sci. 233 (2019) 6026–6050, https://doi.org/10.1177/0954406219858171.
[13] Y. Yang, M. Xu, Y. Du, P. Zhao, Y. Dai, Dynamic analysis of nonlinear time-varying spur gear system subjected to multi-frequency excitation, JVC/J. Vib. Contr. 25 (2019) 1210–1226, https://doi.org/10.1177/1077546318814951.
[14] Y. Yang, L. Cao, H. Li, Y. Dai, Nonlinear dynamic response of a spur gear pair based on the modeling of periodic mesh stiffness and static transmission error, Appl. Math. Model. 72 (2019) 444–469, https://doi.org/10.1016/j.apm.2019.03.026.
[15] Z. Wang, L. Zhang, Y.Q. Luo, C.Z. Chen, Dynamic model of spur gear pair with modulation internal excitation, Int. J. Rotating Mach. (2017), https://doi.org/10.1155/2017/1264904.
[16] H. Motahar, F.S. Samani, M. Molaie, Nonlinear vibration of the bevel gear with teeth profile modification, Nonlinear Dynam. 83 (2016) 1875–1884, https://doi.org/10.1007/s11071-015-2452-z.
[17] J. Yang, T. Lim, Dynamics of coupled nonlinear hypoid gear mesh and time-varying bearing stiffness systems, SAE Int. J. Passeng. Cars - Mech. Syst. 4 (2011) 1039–1049, https://doi.org/10.4271/2011-01-1548.
[18] J. Wang, T.C. Lim, Effect of tooth mesh stiffness asymmetric nonlinearity for drive and coast sides on hypoid gear dynamics, J. Sound Vib. 319 (2009) 885–903, https://doi.org/10.1016/j.jsv.2008.06.021.
[19] V.K. Ambarisha, R.G. Parker, Nonlinear dynamics of planetary gears using analytical and finite element models, J. Sound Vib. (2007), https://doi.org/10.1016/j.jsv.2006.11.028.
[20] M. Zhao, J.C. Ji, Nonlinear torsional vibrations of a wind turbine gearbox, Appl. Math. Model. 39 (2015) 4928–4950, https://doi.org/10.1016/j.apm.2015.03.026.

[21] X. Qiu, Q. Han, F. Chu, Investigation of parametric instability of the planetary gear under speed fluctuations, Shock Vib. 2017 (2017), https://doi.org/10.1155/2017/6851903.
[22] C. Gill-Jeong, Nonlinear behavior analysis of spur gear pairs with a one-way clutch, J. Sound Vib. (2007), https://doi.org/10.1016/j.jsv.2007.01.044.
[23] C. Gill-Jeong, Numerical study on reducing the vibration of spur gear pairs with phasing, J. Sound Vib. (2010), https://doi.org/10.1016/j.jsv.2010.04.005.
[24] G. Bonori, F. Pellicano, Non-smooth dynamics of spur gears with manufacturing errors, J. Sound Vib. (2007), https://doi.org/10.1016/j.jsv.2007.05.013.
[25] S. Wei, Q.K. Han, X.J. Dong, Z.K. Peng, F.L. Chu, Dynamic response of a single-mesh gear system with periodic mesh stiffness and backlash nonlinearity under uncertainty, Nonlinear Dynam. (2017), https://doi.org/10.1007/s11071-017-3435-z.
[26] T.C. Kim, T.E. Rook, R. Singh, Effect of smoothening functions on the frequency response of an oscillator with clearance non-linearity, J. Sound Vib. (2003), https://doi.org/10.1016/S0022-460X(02)01469-4.
[27] A. Farshidianfar, A. Saghafi, Global bifurcation and chaos analysis in nonlinear vibration of spur gear systems, Nonlinear Dyn. Int. J. Nonlinear Dyn. Chaos Eng. Syst. ISSN Nonlinear Dyn. (2014) 783–806, https://doi.org/10.1007/s11071-013-1104-4, 0924.
[28] X.F. Gou, L.Y. Zhu, D.L. Chen, Bifurcation and chaos analysis of spur gear pair in two-parameter plane, Nonlinear Dynam. 79 (2014) 2225–2235, https://doi.org/10.1007/s11071-014-1807-1.
[29] Y. Li, T. Chen, X. Wang, Non-linear dynamics of gear pair with dynamic backlash subjected to combined internal and external periodic excitations, JVC/J. Vib. Contr. 22 (2016) 1693–1703, https://doi.org/10.1177/1077546314544350.
[30] S. Theodossiades, S. Natsiavas, On geared rotordynamic systems with oil journal bearings, J. Sound Vib. 243 (2001) 721–745, https://doi.org/10.1006/jsvi.2000.3430.
[31] S. Baguet, G. Jacquenot, Nonlinear couplings in a gear-shaft-bearing system, Mech. Mach. Theor. 45 (2010) 1777–1796, https://doi.org/10.1016/j.mechmachtheory.2010.08.009.
[32] R. Fargère, P. Velex, Influence of clearances and thermal effects on the dynamic behavior of gear-hydrodynamic journal bearing systems, J. Vib. Acoust. Trans. ASME 135 (2013), https://doi.org/10.1115/1.4025018.
[33] Z. Liu, Z. Liu, J. Zhao, G. Zhang, Study on interactions between tooth backlash and journal bearing clearance nonlinearity in spur gear pair system, Mech. Mach. Theor. 107 (2017) 229–245, https://doi.org/10.1016/j.mechmachtheory.2016.09.024.
[34] S. Kim, A.B. Palazzolo, Shooting with deflation algorithm-based nonlinear response and Neimark-Sacker bifurcation and chaos in floating ring bearing systems, J. Comput. Nonlinear Dynam. 12 (2017) 1–15, https://doi.org/10.1115/1.4034733.
[35] S. Kim, A.B. Palazzolo, Effects of thermo hydrodynamic (THD) floating ring bearing model on rotordynamic bifurcation, Int. J. Non Lin. Mech. 95 (2017) 30–41, https://doi.org/10.1016/j.ijnonlinmec.2017.05.003.
[36] S. Kim, A.B. Palazzolo, Bifurcation analysis of a rotor supported by five-pad tilting pad journal bearings using numerical continuation, J. Tribol. 140 (2018) 1–12, https://doi.org/10.1115/1.4037699.
[37] D. Shin, A. Palazzolo, Multiple Steay State Response Solver for Nonlinear Gear, Bearing and Mafunction Simulation, Texas A&M University, College Station, TX, USA, 2017. Techincal report no. TRC-400124-00073.
[38] Q. Ma, A. Kahraman, Subharmonic resonances of a mechanical oscillator with periodically time-varying, piecewise-nonlinear stiffness, J. Sound Vib. (2006), https://doi.org/10.1016/j.jsv.2005.11.026.
[39] J. Wang, T.C. Lim, M. Li, Dynamics of a hypoid gear pair considering the effects of time-varying mesh parameters and backlash nonlinearity, J. Sound Vib. 308 (2007) 302–329, https://doi.org/10.1016/j.jsv.2007.07.042.
[40] L. Xiang, Y. Jia, A. Hu, Bifurcation and chaos analysis for multi-freedom gear-bearing system with time-varying stiffness, Appl. Math. Model. 40 (2016) 10506–10520, https://doi.org/10.1016/j.apm.2016.07.016.
[41] S. Zhou, G. Song, M. Sun, Z. Ren, Nonlinear dynamic response analysis on gear-rotor-bearing transmission system, JVC/J. Vib. Contr. 24 (2018) 1632–1651, https://doi.org/10.1177/1077546316667178.
[42] Ali H. Nayfeh, Balakumar Balachandran, Applied Nonlinear Dynamics: Analytical, Computational, and Experimental Methods, John Wiley & Sons, 2008.